

UCLA

UCLA Electronic Theses and Dissertations

Title

Design of a Hard X-ray Spectrometer to Demonstrate Novel X-ray Technologies

Permalink

<https://escholarship.org/uc/item/6k1313bv>

Author

Kim, Isaiah

Publication Date

2024

Peer reviewed|Thesis/dissertation

UNIVERSITY OF CALIFORNIA
Los Angeles

Design of a Hard X-ray Spectrometer to Demonstrate Novel X-ray Technologies

A thesis submitted in partial satisfaction
of the requirements for the degree
Master of Science in Electrical and Computer Engineering

by

Isaiah Kim

2024

© Copyright by

Isaiah Kim

2024

ABSTRACT OF THE THESIS

Design of a Hard X-ray Spectrometer to Demonstrate Novel X-ray Technologies

by

Isaiah Kim

Master of Science in Electrical and Computer Engineering

University of California, Los Angeles, 2024

Professor Sergio Carbajo, Chair

Recent developments in the field of ultrafast X-ray science have been accompanied by significant advancements in ultrafast table-top laser technologies as various research groups have built table-top beamlines to conduct experiments that were previously only possible at large synchrotron facilities. At the Quantum Light-Matter Cooperative (QLMC), we are interested in leveraging these scientific advancements to study novel methods of shaping electron wavepackets to generate enhanced bremsstrahlung radiation. This thesis details the full design and future developmental plans of a hard X-ray spectrometer that will become a vital element of the QLMC table-top beamline as we study X-ray generation. This spectrometer will operate outside of vacuum and will be composed of a silicon crystal diffraction grating and a Timepix3 hybrid pixel detector. This thesis delves into the physical principles that underpin both of these key spectrometer components as well as their roles in enabling an effective energy-dispersive X-ray spectrometer. Simulated energy distributions based on the design of this spectrometer ultimately demonstrate its ability to cover a photon energy range of 6.12 to 27.8 keV while also possessing the ability to probe narrower energy ranges with less than 0.1% energy resolution.

The thesis of Isaiah Kim is approved.

Kang L. Wang

Chee Wei Wong

Sergio Carbajo, Committee Chair

University of California, Los Angeles

2024

To my loving family

Contents

Abstract	ii
List of Figures	vii
Acknowledgements	xi
1 Introduction	1
1.1 The Quantum Light-Matter Cooperative	4
1.2 Novel X-ray Generation	9
1.3 Building a Hard X-ray Spectrometer	11
2 The Silicon Crystal Diffraction Grating	13
2.1 X-ray Diffraction and Bragg's Law	15
2.2 Crystallographic Planes	17
2.3 Hard X-ray Spectrometers in Literature	19
2.4 Silicon Crystal Selection	22
3 The Timepix3 Detector	24
3.1 Hybrid Pixel Detector Structure	25
3.2 Particle Detection Principles	27
3.3 The Timepix3 Chip	28
3.4 The Timepix3 Detector at the QLMC	31
3.5 Electron Detection using the Timepix3	33
3.6 X-ray Detection using the Timepix3	35
3.7 SoPhy Control Software	37
3.8 Preliminary Measurement of Background Radiation	41
4 X-ray Spectrometer Design	43
4.1 A Conceptual Base Case - The Silicon Monochromator	45
4.2 The Full X-ray Spectrometer	47
4.3 Simulating the Energy Distribution	51
4.4 X-ray Spectrometer Calibration	59
4.5 Items to Purchase	61
5 Outlook and Future Plans	63
5.1 Summary	63
5.2 Future Work	64

5.3 Outlook 65

List of Figures

1.1	A 3D rendered model of our beamline, including (from right to left) the vacuum pumping system, the electron gun, the electron bunch shaping coils, and the chambers holding the tungsten target, phosphorus screen, and Faraday cup. .	5
1.2	Schematic depiction of the 100 kV DC photogun, including labels for many of the key components as well as a magnified diagram of the parts holding the anode and cathode [40].	5
1.3	Focusing (left) and steering (right) coils that are used for shaping the generated electron bunches [52, 54].	7
1.4	Visual explanation of longitudinal compression of an electron bunch in an RF cavity [40]. From top to bottom, the RF cavity is increasing phase within an RF cycle, and there is an electron bunch that is expanding as it approaches the cavity while the force due to the RF field in the cavity points opposite the bunch movement. The force is zero when the bunch is inside the cavity. Later, as the bunch exits the cavity, the force has flipped sign and now accelerates the electrons at the back of the bunch, causing them to effectively catch up to the frontmost electrons and compress the bunch.	8
1.5	Results of theoretical computations that demonstrate the enhanced directionality of atomic bremsstrahlung radiation via electron waveshaping [51]. (a) and (b) illustrate the difference between a typical single-state electron that induces bremsstrahlung emission via interactions with a carbon atom and a multi-state electron that has been shaped before it interacts with matter. (c-j) are visualizations of the difference between the bremsstrahlung emission angular distributions for 1-state, 2-state incoherent, and 2-state coherent electrons for both 20 and 200 keV energies. These figures clearly demonstrate the stronger on-axis (directional) emission resulting double-state coherent electrons that are able to undergo quantum interference.	10
2.1	Diagram depicting the path length differences (in green) that arise between parallel rays of a plane wave that hits the grooves of a diffraction grating. . .	14
2.2	Diagram depicting the path length differences (in green) that arise between parallel rays of a plane wave that hits the atoms in a crystal lattice.	16
2.3	Plot showing the scattering angles (Bragg angles) that satisfy the Bragg condition for X-ray energies ranging from 5 to 30 keV for various crystallographic planes within a silicon crystal.	19

2.4	Schematic of the HXR spectrometer at the LCLS, which includes a bent silicon crystal and a scintillator-based detection system. Arrows highlight the degrees of freedom of different components for energy tuning purposes and other adjustments [43].	20
2.5	Schematic of the HXR spectrometer at the MuCLS, which includes a divergent X-ray source, a silicon crystal, and a scintillator-based detection system [25].	21
2.6	Plot of the transmission of hard X-rays with energies from 5 to 30 keV through a silicon wafer with thickness 100 μm using data from [24].	23
3.1	(a) Simplified diagram of a silicon sensor, which can be represented by a p-n junction with a depletion zone extended by the bias voltage [46]. (b) Diagram of a single pixel of the detector which shows how when a particle hits the silicon sensor, it creates electron-hole pairs that move toward the electronics chip bump-bonded to the sensor [44]. (c) Schematic diagram of the entire detector chip, including not only the electronics chip and the silicon sensor but also the pixel implant that underlies the pixelated detection system [44].	26
3.2	Plot depicting the photon absorption coefficient in silicon as a function of photon energy [46]. Depending on the photon energy, there are different mechanisms of absorption that are dominant. At the lower end of energies on this plot, which is our X-ray energy range of interest, it is clear that photoelectric absorption dominates.	28
3.3	Plot of the nonlinear calibration function relating time over threshold (ToT) to particle energy for a single Timepix3 pixel [29]. Because each individual pixel possesses independent analog electronics, there effectively are 65,536 independent channels that must be calibrated using this function [28]. This dependence is modeled by equation (3.1).	30
3.4	Image of our quad Timepix3 detector with its full housing connected to several important cables. The red and blue cables in the foreground are tubes that connect to the liquid chiller so that the detector's electronics board can be maintained around room temperature. The black, sky blue, and blue cables are power, fiber optic, and Ethernet cables, respectively. There is also an external SmarAct control unit visible in the right side of the image, and that is used for controlling the mechanical aluminum shutter above the detector chip.	32
3.5	3D rendered model of our beamline, which now has the Timepix3 detector connected to the end. This configuration will be used for electron bunch measurements.	34
3.6	Labeled screenshot of the main control window of SoPhy [5].	39
3.7	Screenshots of the DAC and advanced detector settings, where many of the most important detector parameters can be adjusted [5].	40
3.8	Background radiation in the lab as detected by the Timepix3 detector via SoPhy over a 100 second integration period. This measurement not only demonstrates that the Timepix3 detector is functioning as expected, but also highlights the various types of radiation (alpha particles, cosmic rays, etc.) that will always be present in the background.	42

3.9	Examples of pixel cluster patterns that are generated by different types of particles. These were defined in experiments using the Medipix2 detector, but are still detected in the same patterns in Timepix3 detectors [11].	42
4.1	Schematic diagram (not to scale) detailing the design of our HXR spectrometer from a top-down view, including the electrons hitting the tungsten (W) target to emit bremsstrahlung radiation, which then travels out of the vacuum chamber toward the silicon crystal and then to the Timepix3 detector. Dashed lines/arrows represent crystal rotation and detector revolution to access different energy ranges and/or crystallographic planes.	43
4.2	Plot of the transmission of hard X-rays with energies from 5 to 30 keV through air over a path length of 14 cm using data from [24].	44
4.3	Simplified diagram of a monochromator based around the same design as our spectrometer, except relying on a single ray of photons hitting the crystal as opposed to a diverging beam. Important components and angles are labeled.	45
4.4	Three snapshots of the Bragg reflection interaction at the silicon crystal, each with differing crystal rotation angles and, hence, differing Bragg angles and differing selected X-ray energy (decreasing energy from left to right snapshots).	47
4.5	An update to Figure 4.3 to display the spectrometer setup which includes a diverging X-ray beam with divergence α and central ray energy E_0 , which corresponds to a Bragg angle of $\theta_{B,0}$	48
4.6	Circular cross section of the diverging X-ray beam placed in the context of a uniquely defined coordinate system that quantifies all of the beam's rays by its angular divergence from the axes in both horizontal and vertical directions. For example, the ray passing through C has α_x and α_y coordinates equal to the angle between the ray passing through A and the ray passing through D and B , respectively.	49
4.7	Simulated plots visualizing the X-ray energy distribution and per-pixel energy resolution at the detector as dispersed by the (100) plane with central ray energy 10 keV. The color bar is meant to be similar to the colors of the visible wavelength range, which range from red (low photon energy) to violet (high photon energy), to visualize the varying X-ray energies, although X-rays are not actually physically visible in colors we can perceive.	53
4.8	Simulated plots visualizing the X-ray energy distribution and per-pixel energy resolution at the detector as dispersed by the (300) plane with central ray energy 10 keV.	54
4.9	Simulated plots visualizing the X-ray energy distribution and per-pixel energy resolution at the detector as dispersed by the (500) plane with central ray energy 21 keV.	55
4.10	Simulated plots visualizing the X-ray energy distribution and per-pixel energy resolution at the detector as dispersed by the (800) plane with central ray energy 21 keV.	56

4.11	Simulated plots visualizing the X-ray energy distribution and per-pixel energy resolution at the detector as dispersed by the (100) plane with central ray energy 10 keV, but this time with a 16 cm distance between the X-ray source and the silicon crystal as opposed to 12 cm.	57
4.12	Simulated plots visualizing the X-ray energy distribution and per-pixel energy resolution at the detector as dispersed by the (100) plane with central ray energy 10 keV, but this time with a 14 cm distance between the X-ray source and the silicon crystal as opposed to 12 cm as well as a 2 mm distance between the crystal and the detector as opposed to 2 cm.	58
4.13	Plot of the transmission of hard X-rays with energies from 5 to 30 keV through a copper foil with thickness 20 μm using data from [24].	60

Acknowledgements

First and foremost, I would like express my deepest gratitude for Prof. Sergio Carbajo for his invaluable guidance and support during my time as a student in his lab. I am eternally grateful for the warmth with which he first welcomed me into the QLMC and the field of ultrafast science as well as the great opportunities he provided me to conduct research in this field for my master's thesis.

I would also like to thank Prof. Chee Wei Wong and Prof. Kang L. Wang for their time and effort toward being vital members on my thesis committee as well as for being great professors in the solid state electronics courses I took under their instruction.

I truly appreciate the support from Abbas Shiri and Brittany Lu for their mentorship and friendship during my time as a student in the QLMC and for all the many fruitful discussions we shared about my project.

I am also very grateful for Juan José Latorre for being a wonderful labmate and helping me obtain high-quality 3D rendered models of our beamline.

I would also like to extend my sincerest appreciation to Eric van Genderen for all of his guidance and advice with everything surrounding the Timepix3 hybrid pixel detector, without which my project would never have been possible.

Finally, a special thanks to my loving parents, my brother, and my dog for their unwavering love and support for me as I worked through the the master's program at UCLA.

Chapter 1

Introduction

The discovery of X-rays by Wilhelm Röntgen in 1895 marked a monumental scientific breakthrough, ultimately revolutionizing our understanding of matter through their pivotal role in a wide range of unique experiments. X-rays and their applications have since contributed to the work behind over 25 Nobel Prizes across various disciplines, highlighting their extensive impact scientific research. The broad applicability and significance of X-rays can be attributed to their ultrashort wavelengths allowing atomic-scale interactions with matter, their high transmission through many materials enabling novel X-ray imaging, and the chemical applicability of X-ray spectroscopy allowing the study of complex chemical structures.

Over the last several decades, the development of synchrotron-based X-ray sources has heralded a new era of X-ray science [45]. By leveraging the technology of high-energy particle accelerators, these sources are able to generate X-ray beams that not only possess high intensity and directionality, but also can operate over a large range of wavelengths. Alongside these developments, the field of ultrafast science has also grown significantly due primarily to remarkable progress in table-top laser technology, including efforts to push toward shorter and shorter wavelengths.

There have been two key methods utilizing the strong field interaction that have been

studied for developing ultrafast table-top lasers in the X-ray wavelength range (from less than 0.1 to a few nanometers): laser-produced plasmas [38], which produce femtosecond pulses of incoherent hard X-rays, and high-order harmonic generation [33], which produces femto- to attosecond pulses of coherent XUV. Furthermore, the use of relativistic electron beams in conjunction with continuously advancing laser technology has led to the development and usage of ultrafast X-ray sources at prominent synchrotron-based X-ray source facilities around the world [45]. These expansions have aimed to simultaneously harness the benefits of both X-rays and ultrafast science to study matter at the atomic scale via scattering while also being able to access the fundamental timescales of electronic and atomic motion, with an ultimate objective of attaining a greater comprehensive understanding of the functional and structural properties of matter.

Perhaps one of the most important inventions that have resulted from ultrafast X-ray science research has been the X-ray free-electron laser (XFEL). These lasers can produce tunable, coherent X-ray beams that are many orders of magnitude brighter than any previously available source as well as possess ultrashort pulse durations in the femto- and even subfemtosecond regimes. They are based on free-electron lasers (FELs), which were first first devised and demonstrated at Stanford University in the 1970s [17]. These devices pass electron bunches through a magnetic structure known as an undulator to generate radiation, which then interacts back again with the electrons to make them emit coherently, inducing amplification of coherent electromagnetic radiation.

While the first FELs operated in the infrared wavelength range [17], later efforts pushed toward EUV (extreme ultraviolet) and X-ray radiation, which initially proved to be difficult due to underlying physical principles that prevent efficient operation of traditional lasers at these shorter wavelengths [19]. To circumvent these limitations, a bright electron beam propagating through an additional long undulator can be used to further amplify the initial spontaneous electromagnetic radiation from the relativistic electrons in the FEL undulator, leading to self-amplified spontaneous emission (SASE) of intense, quasi-coherent radiation

[32]. XFELs operating in the SASE mode have demonstrated generation of multi-gigawatt, femtosecond pulses of coherent X-ray radiation, highlighting their ability to surpass the powerful sources offered by synchrotron-based sources. As a result, XFELs have risen to the forefront of ultrafast science with their great potential as powerful probes for both the ultrasmall and ultrafast realms.

XFELs and their powerful applications for innovative X-ray science have led to the rise of large-scale XFEL sources at prominent facilities around the world. The initial demonstrations of these impactful X-ray sources and their immense scientific potential were spearheaded by four primary facilities: FLASH (Free electron LASer in Hamburg) at the Deutsches Elektronen-Synchrotron [6], which was the world's first XFEL developed for operation in the EUV and SXR (soft X-ray) spectral ranges; LCLS (Linac Coherent Light Source) at SLAC National Accelerator Laboratory [9], which was the first HXR (hard X-ray) XFEL and became the most powerful X-ray source in the world; FERMI (Free Electron laser Radiation for Multidisciplinary Investigations) in Trieste [2], which was the first seeded EUV XFEL; and SACLA (SPring-8 Angstrom Compact free Electron LASer) in Japan [27]. Other prominent laser facilities that followed these first generation developments include the Pohang accelerator laboratory in Korea [30], the SwissFEL in Switzerland [22], and the EuXFEL in Germany [3]. Most of these large facilities are based on GeV-scale electron beams generated by standard pulsed-RF accelerator technology; FLASH and EuXFEL are two notable exceptions that have been built upon pulsed superconducting RF (SCRF) accelerator technology.

The LCLS at SLAC first began lasing in 2009, and was particularly noteworthy for the world of X-ray science due to its pioneering operation in the HXR spectral range, at around 1.5 Angstroms wavelength [20]. X-rays across a wide energy range are generated through the SASE process from a single fixed-gap undulator array, leading to pulse durations adjustable in the range of 2-500 fs with energies up to 6 mJ per pulse [18]. Furthermore, more recent work has demonstrated the generation of pulses with subfemtosecond duration using nonlinear e-bunch compression techniques [26].

One significant upgrade has been successfully implemented at the LCLS with another on the way. The former is known as LCLS-II, which introduced a 4 GeV SCRF accelerator to accelerate electrons to high energies with nearly zero loss and ultimately enable generation of up to a million X-ray pulses per second with energies in the 0.25-5 keV range [7, 45]. LCLS-II was commissioned in 2022 and is now hosting experiments with unprecedented precision to study a myriad of scientific subjects, including quantum materials to research novel computing and communications methods, volatile chemical processes to push for the creation of sustainable clean energy technologies, and vital biological compounds to motivate the development of new medicinal drugs. The second upgrade, still under development, is known as LCLS-II-HE (High Energy) and aims to double the electron beam energy of the SCRF accelerator used by LCLS-II to 8 GeV and consequently increase the spectral maximum of the XFEL to upwards of 12 keV, and potentially eventually beyond 18 keV, at the same high repetition rate [45].

1.1 The Quantum Light-Matter Cooperative

Building on the advances at the LCLS, our research group at the Quantum Light-Matter Cooperative (QLMC) based at the University of California, Los Angeles both initiates independent projects and collaborates closely with researchers at the LCLS to extend the frontiers of ultrafast science. While the LCLS provides access to high-energy, high-repetition rate X-rays for large-scale experiments, our lab is interested in complementary investigations in a table-top setting, exploring laser and accelerator physics at the intersection of free electrons and X-rays. Some key planned scientific projects include single-electron photon-induced near-field electron microscopy studies and non-relativistic electron-photon QED experiments, the latter of which directly relevant to the work presented in this thesis.

Our current laboratory setup, which is displayed in the 3D rendered image in Figure 1.1, begins with a DC photogun (see Figure 1.2) which is used to generate and accelerate electron

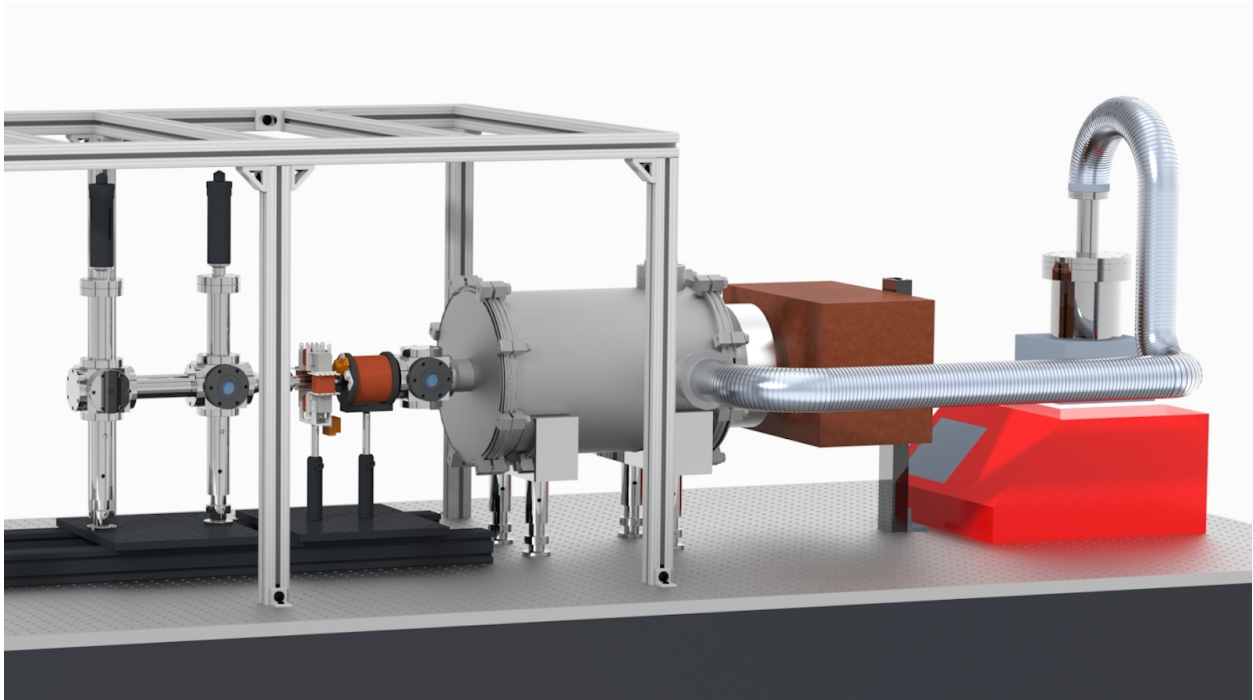


Figure 1.1: A 3D rendered model of our beamline, including (from right to left) the vacuum pumping system, the electron gun, the electron bunch shaping coils, and the chambers holding the tungsten target, phosphorus screen, and Faraday cup.

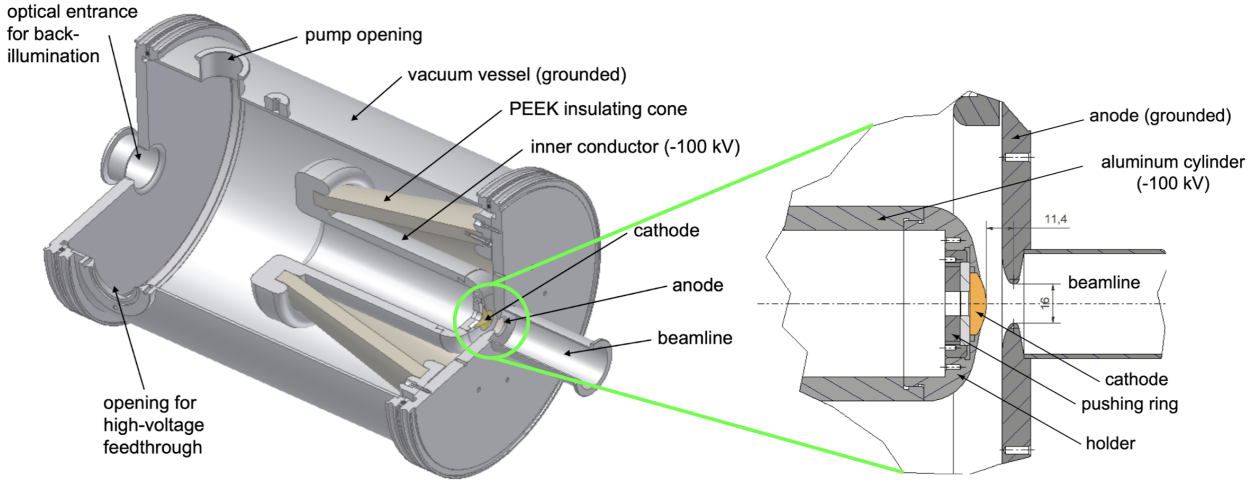


Figure 1.2: Schematic depiction of the 100 kV DC photogun, including labels for many of the key components as well as a magnified diagram of the parts holding the anode and cathode [40].

bunches in vacuum. Voltages up to 100 kV can be applied across a cathode and anode containing a hole within the photogun, resulting in up to a 12 MV/m DC electric field on the cathode surface [53]. Electron bunches are typically generated by front illumination of a bulk copper cathode through the anode hole, but can also be generated via back illumination using a glass cathode with a thin copper deposition on top, with the latter case being easier to align. However, bulk copper offers a greater quantum efficiency than copper coating, thus our photogun currently uses a bulk copper cathode, yielding greater efficiency in our electron generation process. To achieve photoemission, we currently use a PHAROS femtosecond laser at 1030 nm to pump a HIRO harmonic generator, both of which are manufactured by Light Conversion, which provides very efficient fourth harmonic output pulses at 258 nm with pulse durations around 200 fs. These UV pulses illuminate the bulk copper cathode in the photogun to photoemit ultrashort electron bunches, which are then accelerated by the DC electric field out of the gun through the anode hole.

Following the aforementioned electron bunch generation, multiple steps can be taken to ensure proper shaping of these bunches in both time and space to allow precisely controlled electron-matter interactions further down the beamline. The first of these mechanisms is a magnetic focusing coil mounted directly to the exit of the electron gun that generates a strong magnetic field along the propagation direction of the electrons [54]. This magnetic field focuses the electron bunches, which are typically subject to strong Coulomb expansion at the charge range we expect to generate. As a result, this focusing coil allows for precise transverse focusing of the beam onto any sample, target, or detector. On the other hand, a steering coil, composed of four individual coils arranged in a square geometry around the beamline, can be used to steer the electron beam using a magnetic field perpendicular to the beam [52]. If equal currents are sent through opposing pairs of coils, this perpendicular magnetic field enables electron beam deflection perpendicular to the propagation axis. If all four coils have equal currents running through them such that the magnetic field is zero along the propagation axis, the steering coil acts as a quadrupole lens, which can focus the electron

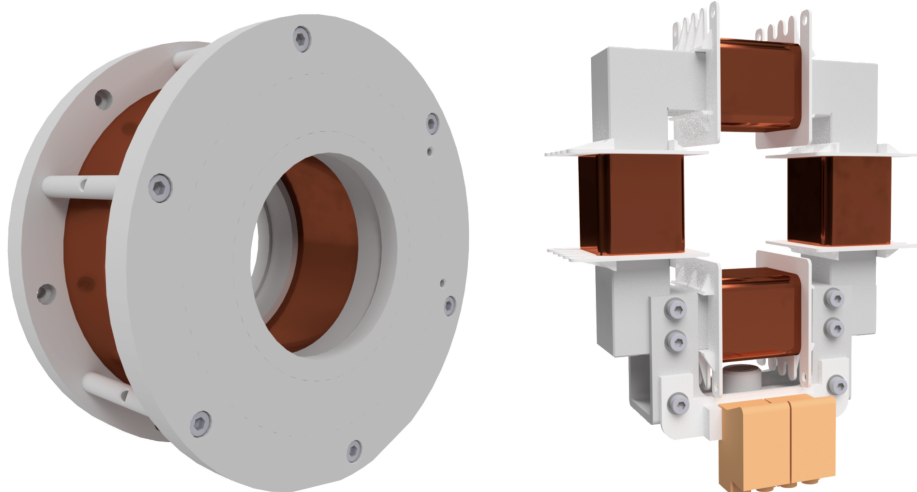


Figure 1.3: Focusing (left) and steering (right) coils that are used for shaping the generated electron bunches [52, 54].

bunches in one direction perpendicular to the axis while simultaneously letting the bunches expand in the other direction. This can be useful for creating a line focus or for correcting any potential beam astigmatism. These two types of coils are displayed in Figure 1.3.

While these two previously described components serve as methods of spatially shaping the electron beam, a radio-frequency (RF) cavity can also be added for RF temporal compression of the accelerated electron bunches. When this cavity is operating in a transverse-magnetic mode with an electric field polarized along the beamline axis, the cavity essentially becomes a temporal lens, which is depicted in Figure 1.4 for an arbitrary electron bunch [14]. The front of the bunch enters the cavity at a phase in the RF cycle when the electric field is positive, inducing a retarding force on the electrons at the front of the bunch. When the middle of the bunch enters the cavity, the electric field is zero and, as a result, there is no change in momentum for these electrons. When the electrons at the back of the bunch enter the cavity, however, the electric field is negative and an accelerating force is exerted on these electrons in their direction of propagation. Consequently, the electrons experience greater deceleration the closer they are to the front of the bunch and greater acceleration the closer they are to the back, leading to longitudinal compression of the electron bunch along the beamline axis [40].

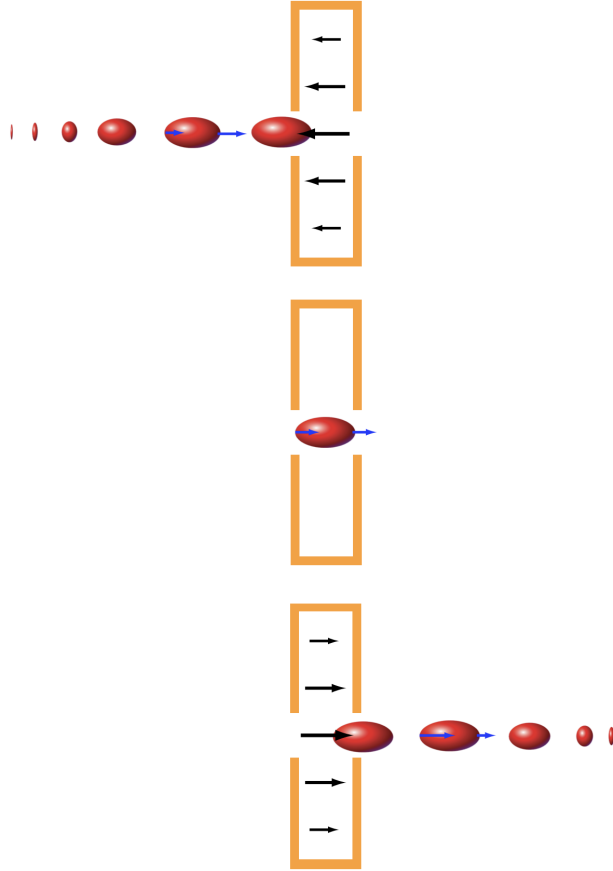


Figure 1.4: Visual explanation of longitudinal compression of an electron bunch in an RF cavity [40]. From top to bottom, the RF cavity is increasing phase within an RF cycle, and there is an electron bunch that is expanding as it approaches the cavity while the force due to the RF field in the cavity points opposite the bunch movement. The force is zero when the bunch is inside the cavity. Later, as the bunch exits the cavity, the force has flipped sign and now accelerates the electrons at the back of the bunch, causing them to effectively catch up to the frontmost electrons and compress the bunch.

Using a combination of these three mechanisms allows for basic electron bunch shaping to allow for various unique experiments, including those involving X-ray generation.

1.2 Novel X-ray Generation

Recent developments in quantum electrodynamics (QED) have explored similar electron waveshaping methods and their ability to potentially enable control over fundamental QED interactions, including light emission [51]. This research by Wong et. al. extends conventional computations in QED and similar field theories which typically assume that incoming particles are single-momentum states, thereby ignoring any intriguing scattering processes due to coherent superposition states or shaped wavepackets. In fact, by manipulating quantum interference via shaped electron wavepackets, these simulations have demonstrated that it is possible to control emission processes like bremsstrahlung, which is spontaneous emission due to free electrons scattering off a static potential. Specifically, they have shown that free electron waveshaping can be leveraged to control both spatial and spectral distributions of Bremsstrahlung, enhancing their directionality, monochromaticity, and versatility compared to emission from unshaped electrons. A succinct visualization of their theoretical results is shown in Figure 1.5.

In our lab, we are currently aiming to take advantage of this emerging QED theory in conjunction with our electron waveshaping setup to experimentally corroborate the aforementioned theoretical results. Of particular interest is radiation in the HXR regime, the highest energy X-rays, because the spatial resolution necessary to manipulate the phases of these ultrashort wavelength photons is impractical through material fabrication of optical components. Due to the prevalence of Bremsstrahlung in modern X-ray tubes used in various settings including security and medicine, this novel method of controlling X-ray emission carries the potential to revolutionize the modern approach to X-ray science and tackle traditional cost-accessibility tradeoffs in X-ray applications. Furthermore, this new X-ray production

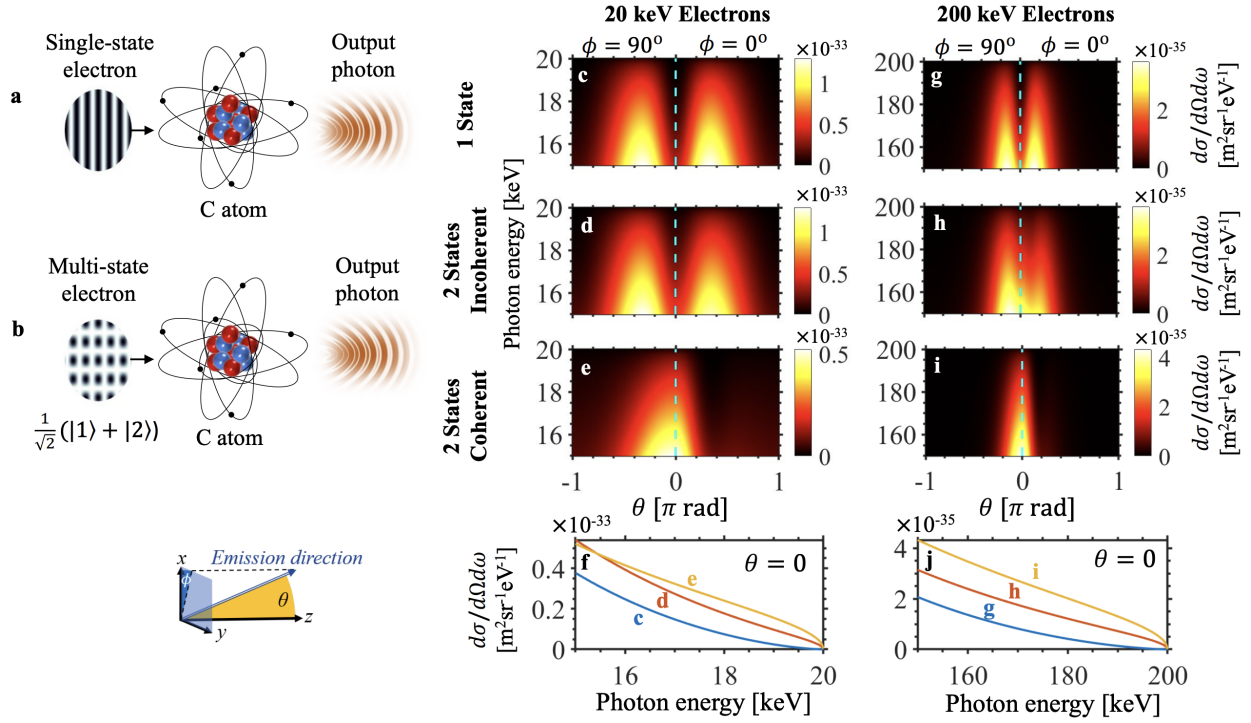


Figure 1.5: Results of theoretical computations that demonstrate the enhanced directionality of atomic bremsstrahlung radiation via electron wavelshaping [51]. (a) and (b) illustrate the difference between a typical single-state electron that induces bremsstrahlung emission via interactions with a carbon atom and a multi-state electron that has been shaped before it interacts with matter. (c-j) are visualizations of the difference between the bremsstrahlung emission angular distributions for 1-state, 2-state incoherent, and 2-state coherent electrons for both 20 and 200 keV energies. These figures clearly demonstrate the stronger on-axis (directional) emission resulting double-state coherent electrons that are able to undergo quantum interference.

regime can open the door for bright and compact radiation sources like portable attosecond XFELs and on-chip accelerators, for example, with greater versatile accessibility for these powerful scientific tools.

This unique coherent multi-state HXR radiation via electron waveshaping has clear, sweeping implications for the advancement of radiation technology, among other applications like absorption spectroscopy and quantum information science. Before these applications are possible, the need to experimentally demonstrate the theoretical QED groundwork of this project and properly benchmark both unshaped and shaped emission characteristics naturally motivates the development of a precise and sensitive HXR spectrometer.

1.3 Building a Hard X-ray Spectrometer

At its core, a spectrometer is a combination of a dispersive element and a detector to measure the intensity and wavelengths of the spectral bands that are produced [13]. Optical spectrometers most commonly utilize a prism or diffraction grating as a dispersive element to angularly separate an incident polychromatic beam into its constituent wavelength components. In a complete setup, this dispersion allows a conveniently placed detector to receive and measure the intensity of these wavelength components contained in a select segment of the electromagnetic spectrum, yielding the spectrometer's spectral measurements. An X-ray spectrometer operates on very similar principles, but the significant difference from optical spectrometers in the wavelengths of photons that are being dispersed and detected introduce some unique physics that must be considered.

In this thesis, I present the design and key conceptual details of an HXR spectrometer for the tabletop beamline at the QLMC. The primary motivation behind this work is to enable spectral analysis in experiments where we aim to demonstrate novel X-ray emission via electron waveshaping as well as build a framework for emerging QED-based compact and portable X-ray sources. In addition, the development of this spectrometer will facilitate

opportunities for a wide range of future X-ray experiments at the QLMC.

This design includes three major chapters. In the first chapter, I review the fundamental physical principles behind diffraction gratings and the design process behind the "diffraction grating" that will be used in this spectrometer. In the second chapter, I introduce the TimePix3 hybrid pixel detector that will be used to detect and measure the X-rays of interest. Specifically, I outline the unique characteristics and physics of the TimePix3 detector and its vital role in analyzing both electrons and X-rays in our beamline. The third chapter integrates the content of the previous two chapters to present the final design and conceptual development behind the complete HXR spectrometer.

Chapter 2

The Silicon Crystal Diffraction Grating

To motivate the foundations of the grating used for this spectrometer design, I first review the fundamental physical concepts surrounding general diffraction gratings, and then later delineate the specific considerations that are required for measuring X-rays.

We recall that for a general optical spectrometer, the typical source of dispersion that separates an incident polychromatic beam into its constituent wavelengths is a prism or a diffraction grating. While a dispersive prism operates on the principle that its material's refractive index depends on the wavelength of light passing through, a grating relies on its periodic structure, as shown in Figure 2.1, to enable diffraction and wave interference, and as I proceed in explaining the essentials of spectrometer physics, I focus on the latter as the dispersive element of choice.

The diagram depicted in Figure 2.1 provides a simplified view of the basic yet intricate physics that happen due to a reflective diffraction grating. A diffraction grating is essentially any structure composed of periodically spaced grooves (for a reflective geometry) or slits (for a transmissive geometry), and this periodic spacing is given as d .

To review the concept of dispersion from a grating, I start with a fundamental base case and assume a plane wave of monochromatic light incident on and scattered by the grating as shown in Figure 2.1 by the black and blue arrows. If I take two parallel rays of this incident

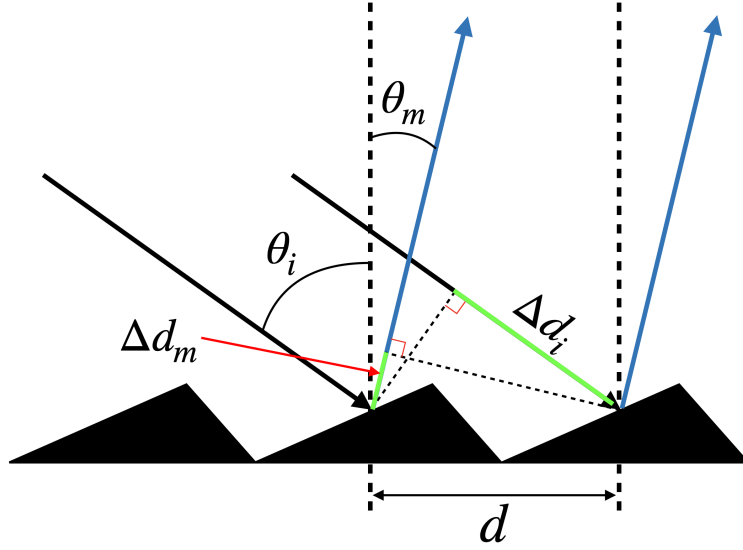


Figure 2.1: Diagram depicting the path length differences (in green) that arise between parallel rays of a plane wave that hits the grooves of a diffraction grating.

beam, like the two black arrows in the diagram, it becomes immediately clear that in order to hit the rightmost groove, the rightmost black arrow must travel an additional path length, Δd_i . By a similar notion, the reflected rays, depicted by blue arrows, also experience a path length difference between them. In this case, the reflected ray from the middle groove travels a length, Δd_m , before it is in line with the reflection point at the rightmost groove. Using trigonometry with the angles, θ_i (incident angle) and θ_m (diffracted angle), defined relative to the grating normal, these path length differences can be written as:

$$\Delta d_i = d \sin \theta_i \quad (2.1)$$

$$\Delta d_m = d \sin \theta_m \quad (2.2)$$

For a given path length difference to result in constructive interference at the detector, the rays must be in phase after the incident light scatters off of the grating. Knowing that the rays must have been in phase before scattering as well, the total path length difference must be equal to an integer multiple of the wavelength, λ , of the incident monochromatic plane wave. Thus, we can use the previously derived path length expressions to obtain a grating

equation for the case visualized in Figure 2.1:

$$\sin \theta_i + \sin \theta_m = \frac{m\lambda}{d} \quad (2.3)$$

where the integer, m , is the order of diffraction. For the rest of this thesis, we will only be discussing the case of $m = 1$, or first order diffraction, because it yields the most intense and most easily detectable diffracted beam. Based on this equation, we can conclude that for a defined wavelength and incident angle, first order constructive interference only occurs for reflections of a defined angle as well. Now, if we consider a polychromatic beam incident on the grating at the same incident angle, θ_i , it becomes apparent that each wavelength contained in the incident beam will be diffracted in a slightly different direction, enabling the grating's dispersive capabilities.

2.1 X-ray Diffraction and Bragg's Law

Unfortunately for X-ray spectroscopy applications, equation (2.3) above presents one key limitation. Conventional gratings typically have spacings on the order of a micron, and we can see that for the visible wavelength range (400 to 700 nm), the ratio on the right hand side of the grating equation is a significant fraction of unity in this case. Consequently, both incident and diffracted angles can be a substantial fraction of the maximum possible angle, resulting in well-defined, easily measurable diffraction patterns. However, when applied to X-rays, whose wavelengths are orders of magnitude smaller, that ratio becomes exceedingly small. Thus, in this wavelength regime, both the incident and diffracted angles would be extremely close to the grating normal, leading to diffraction angles that are nearly impossible to resolve and diminishing any effectiveness of conventional gratings for X-ray spectroscopy. To address this challenge, it is crucial to explore alternative structures with spacings on the order of X-ray wavelengths, allowing for measurable X-ray diffraction and efficient subsequent analysis.

A natural solution is a crystal, whose periodic atomic spacings are very similar to the

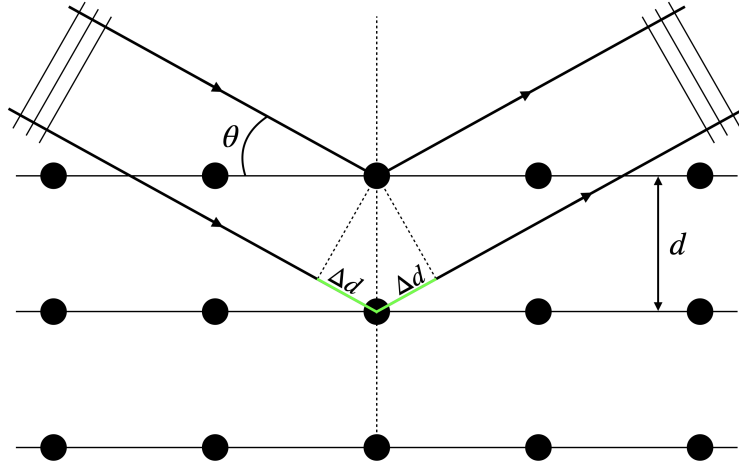


Figure 2.2: Diagram depicting the path length differences (in green) that arise between parallel rays of a plane wave that hits the atoms in a crystal lattice.

probed wavelengths. This idea has its roots in a 1912 discussion where Max von Laue suggested to Paul Peter Ewald, who was studying crystals at the time, that X-rays might possess wavelengths that are comparable to the lattice spacing of crystals, and von Laue subsequently tested this hypothesis [21]. Evidently, after obtaining a clear diffraction pattern using X-rays and a copper sulfate crystal, he confirmed that, indeed, X-rays are a form of electromagnetic radiation with wavelengths that enable diffraction via scattering with atoms in a crystal lattice.

Following this pioneering discovery, physicists William Lawrence Bragg and his father, William Henry Bragg, further researched the light-matter interactions of X-rays and crystals [12]. In particular, they sought to relate the evenly spaced lattice planes of a crystal to the established principles of diffraction to supplement their understanding of how X-rays interact with these periodic structures. This work led to Bragg's law, a relation that describes the angles for coherent scattering of waves due to evenly spaced crystal planes. Figure 2.2 depicts a simplified picture of Bragg scattering from a crystalline solid.

In this depiction, two in-phase rays with the same wavelength interact with a crystal lattice and are each scattered via specular reflection off two atoms within the lattice. Just as with the grating example, it is then immediately clear that the lower ray travels an additional

path length, given by:

$$2\Delta d = 2d \sin \theta \tag{2.4}$$

where d is the lattice plane spacing and θ is the angle of incidence. Constructive interference between these two rays occurs when the path length difference is equal to an integer multiple of the wavelength, which is very similar to the concept behind the grating equation discussed previously. Following that similar logic, we obtain Bragg's Law, or the Bragg condition, describing the condition for constructive interference of rays incident on the crystal:

$$n\lambda = 2d \sin \theta \tag{2.5}$$

where the integer, n , is the order of diffraction. Thus, Bragg's Law serves as a very effective framework by which we can use crystalline structures as diffraction gratings for an X-ray spectrometer.

2.2 Crystallographic Planes

We can extend this idea further to consider distinct families of crystallographic planes within the crystal for Bragg reflection of X-rays. These planes are defined by their Miller indices (hkl) , which represent different planar orientations and periodic spacings within the crystal lattice. For example, the (100) planes correspond to planes parallel to one face of the cubic crystal, each separated from one another by the lattice constant, a . However, these planes are not limited to representing adjacent atomic layers, and many distinct planes can exist within the lattice. In fact, higher-order planes such as (200) , (300) , etc. do not actually describe any unique physical atomic layers, but they still represent a unique symmetry and periodicity within the crystal lattice. As a result, Bragg diffraction uses this periodicity to produce constructive interference, resulting in higher-order Bragg reflections and diffraction peaks.

Regardless of whether the planes are composed of physical atoms, each set of Miller

indices defines a unique family of parallel planes with a specific spacing, d , which is not always equivalent to the nominal lattice constant of the crystal. The effective interplanar spacing, d , used in Bragg's Law is related to the Miller indices and the lattice constant, a , of the cubic crystal by [42, 50]:

$$d = \frac{a}{\sqrt{h^2 + k^2 + l^2}} \quad (2.6)$$

Thus, different sets of crystallographic planes can satisfy the Bragg condition with varying angles of incidence, allowing for the diffraction of different X-ray wavelengths and energies that are reflected at different angles as well. Given a stationary X-ray source and beam, detecting these Bragg-diffracted X-rays may require rotating the crystal and revolving the detector about the crystal. Figure 2.3 depicts how the Bragg condition varies for different X-ray energies and plane families. The X-ray energy range of interest is primarily dictated by the energy of the electrons that we are able to generate from our beamline, which, in turn, is limited by the power supply for the DC photogun. Currently, the maximum voltage output is 60 keV, but we are aiming to keep the voltage at or below 30 keV to ensure safe operation and avoid running too close to the maximum suppliable voltage.

Furthermore, usage of different diffraction planes allows for different energy ranges to be accessed with varying energy resolutions. For one, as evident in the curves presented in Figure 2.3, planes with higher Miller indices have Bragg curves that are steeper (i.e. greater change in Bragg angle) over any given energy range than those of planes with lower Miller indices. As a result, diffraction using high Miller indices enables measurements with greater energy resolution and, thus, the ability to resolve any spectral spikes [43]. At the same time, using low Miller indices is a valid option for obtaining a general idea of the spectrum over a larger energy range without necessarily resolving every individual peak with high precision. However, it is also immediately apparent that the Bragg curves for planes with higher Miller indices simply do not span the lower photon energies, necessitating usage of a combination of planes with lower indices and planes with higher indices to span the entire energy range of

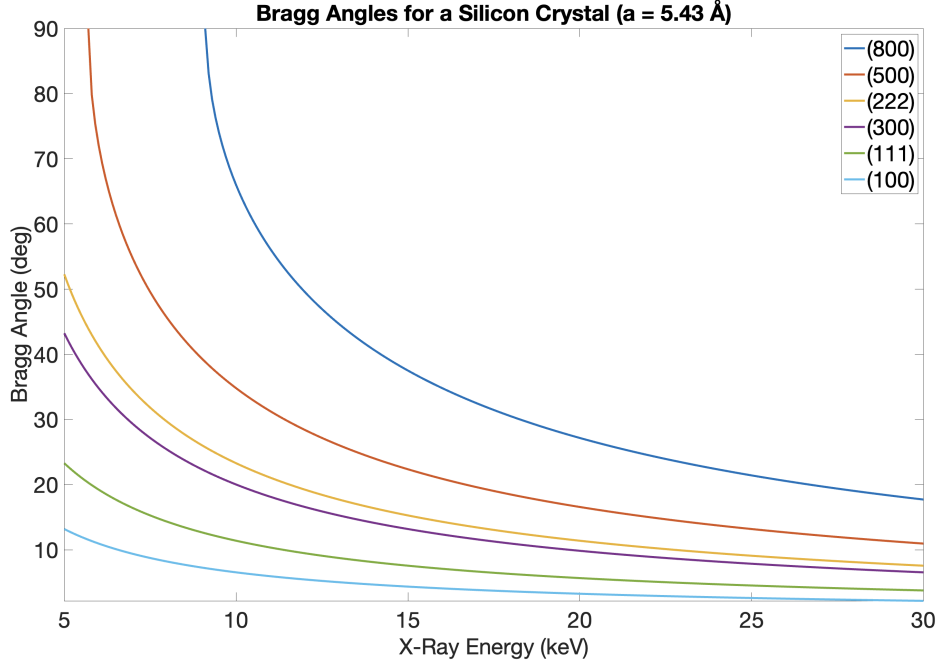


Figure 2.3: Plot showing the scattering angles (Bragg angles) that satisfy the Bragg condition for X-ray energies ranging from 5 to 30 keV for various crystallographic planes within a silicon crystal.

interest with great resolution.

2.3 Hard X-ray Spectrometers in Literature

The concept of utilizing different crystal planes to satisfy the Bragg conditions for a wider range of X-ray energies has been explored by many different research facilities around the world, and they leverage this ability to build spectrometers that operate by the rotation of a single diffraction crystal within it. In the following section, I will discuss two recent examples of energy-dispersive X-ray spectrometers based on Bragg's Law and X-ray diffraction using crystals. Both use a silicon wafer as the diffractive crystal because silicon is an easily accessible crystal with a lattice spacing (0.543 nm) comparable to the wavelength of the hard X-rays being measured. The first of these examples is the LCLS's HXR single-shot spectrometer, while the second is based on similar concepts but utilizes non-collimated X-ray emission as well as a transmissive Laue geometry for diffraction.

To characterize the fluctuations of the XFEL at the LCLS, a team of LCLS researchers developed a variable-energy HXR single-shot spectrometer featuring a cylindrically bent Si thin crystal that disperses the incident highly collimated, polychromatic X-ray beam as well as a spatially resolved detector system made up of a Ce:YAG X-ray scintillator screen that precedes an optical imaging system to measure the resulting spectrum [43]. A bent crystal is used because as the collimated beam strikes the curved surface of the crystal, different parts of the beam encounter different angles relative to the same family of crystal planes, allowing different X-ray energies to satisfy each of those distinct Bragg conditions. As a result, the crystal can selectively diffract X-rays across a range of energies, effectively angularly dispersing the incident beam into a spectrum of the constituent X-ray energies.

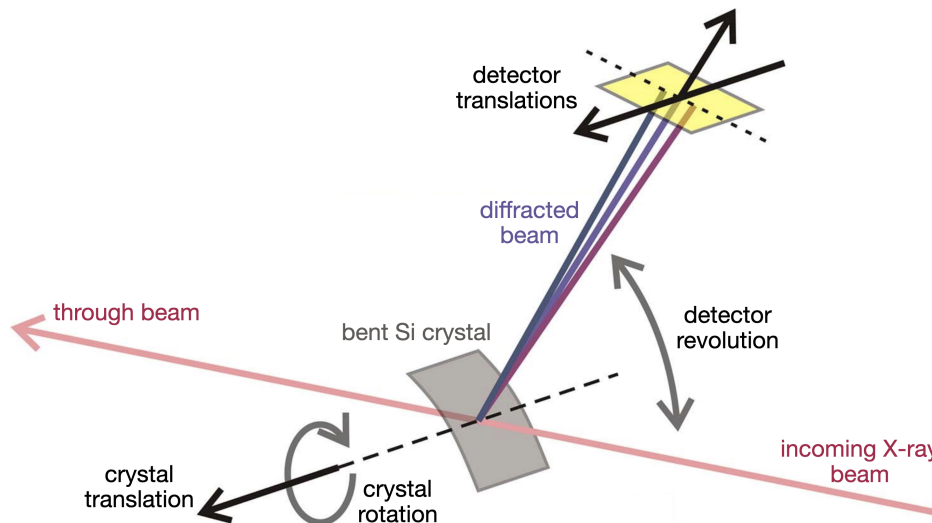


Figure 2.4: Schematic of the HXR spectrometer at the LCLS, which includes a bent silicon crystal and a scintillator-based detection system. Arrows highlight the degrees of freedom of different components for energy tuning purposes and other adjustments [43].

The spectrometer’s basic geometry and motional degrees of freedom for detectable energy tuning are illustrated in Figure 2.4. The spectral measurements from this spectrometer are crucial to experiments that rely heavily on an accurate understanding of the SASE XFEL spectrum, providing valuable insights for accelerator physicists to optimize both the lasing processes and the performance of the HXR FEL at LCLS. By using Si crystals of (220) and (100) cuts, researchers can access the (220), (440), (400), and (800) planes to selectively

diffract X-rays with energies ranging from 4 to 20 keV.

The second example is the X-ray absorption spectroscopy (XAS) setup developed at the Munich Compact Light Source (MuCLS), the world’s first mini synchrotron [25]. Researchers at the MuCLS have developed an inverse Compton scattering (ICS) source to generate highly tunable hard X-rays in a laboratory setting, facilitating advancements in X-ray spectroscopy applications, such as probing the absorption edges of high-Z materials. Their XAS setup includes a slightly bent Si(100) crystal wafer, a CCD camera, a fiber-coupled scintillator, and a commercial energy-dispersive detector to measure the source spectrum.

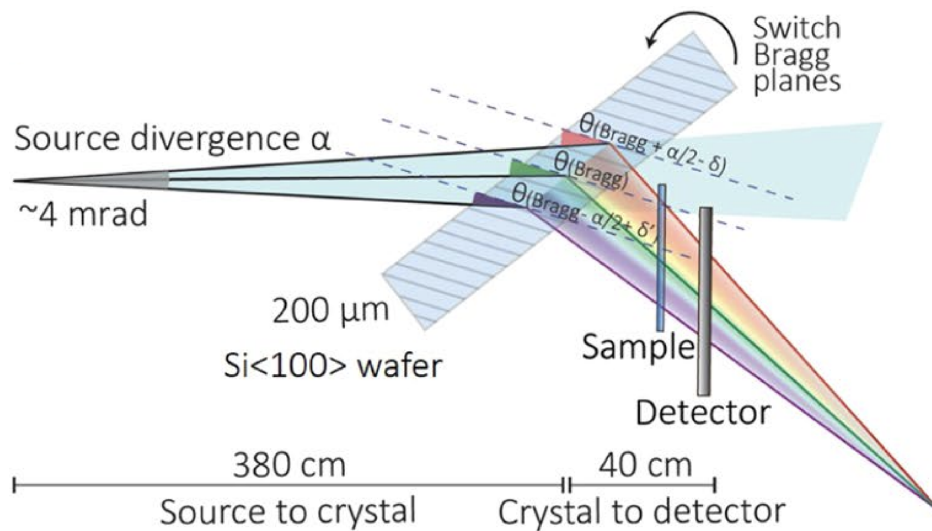


Figure 2.5: Schematic of the HXR spectrometer at the MuCLS, which includes a divergent X-ray source, a silicon crystal, and a scintillator-based detection system [25].

Unlike the spectrometer setup at the LCLS, this setup uses the crystal wafer in a transmissive diffraction grating configuration to mitigate spectrum distortions at higher X-ray energies. Furthermore, unlike the collimated XFEL used at the LCLS, the conic output of the MuCLS’s ICS source allows different parts of the beam to scatter off the selected diffraction plane at different angles, satisfying the Bragg condition for different X-ray energies depending on position within the spot of the beam at the crystal, regardless of whether the crystal is bent. Due to the reflected angles being equal to the Bragg angles of incidence, these reflected beams of different individual energies eventually converge to a spot detectable by the detector.

This concept is explored in further detail later in this thesis as I utilize a similar configuration for the design of our spectrometer. The geometry of the MuCLS setup is depicted in Figure 2.5.

2.4 Silicon Crystal Selection

Building on the precedent of these two designs, I similarly centered the design of our HXR spectrometer around a silicon wafer serving as a diffraction grating in a transmissive Laue geometry to avoid spectral distortion as we generate higher energy bremsstrahlung radiation [23, 25].

Selection of a silicon wafer that would allow maximal transmission of X-rays was a key consideration during the design process because of the transmissive geometry of our diffraction grating configuration. Because the similar transmissive setup at the MuCLS used a silicon wafer with a 200 μm thickness, we aimed to keep our crystal thickness within the same order of magnitude. However, X-ray transmission through silicon, which is plotted in Figure 2.6, sharply decreases below 10 keV, which remains within our desired X-ray energy range. As a result, we sought to maximize transmission particularly at those lower energies while keeping manufacturing costs reasonable. This led to the choice of a 100 μm wafer, which still provides a reasonable $\sim 50\%$ transmission with 10 keV photons and above $\sim 80\%$ for energies greater than 15 keV, making it a suitable and cost-effective option for our spectrometer design.

While other factors like crystal cut and doping were considered, thickness remained the primary concern. Substantial X-ray transmission through the grating was critical, and we selected an option that balanced performance and cost.

Other wafer design characteristics like crystal cut, diameter, and doping were considered but ultimately had less influence than wafer thickness on the decision. Attaining significant X-ray transmission through the grating would be critical for this spectrometer, and we selected an option that balanced thickness and cost for this reason. The crystal that was purchased

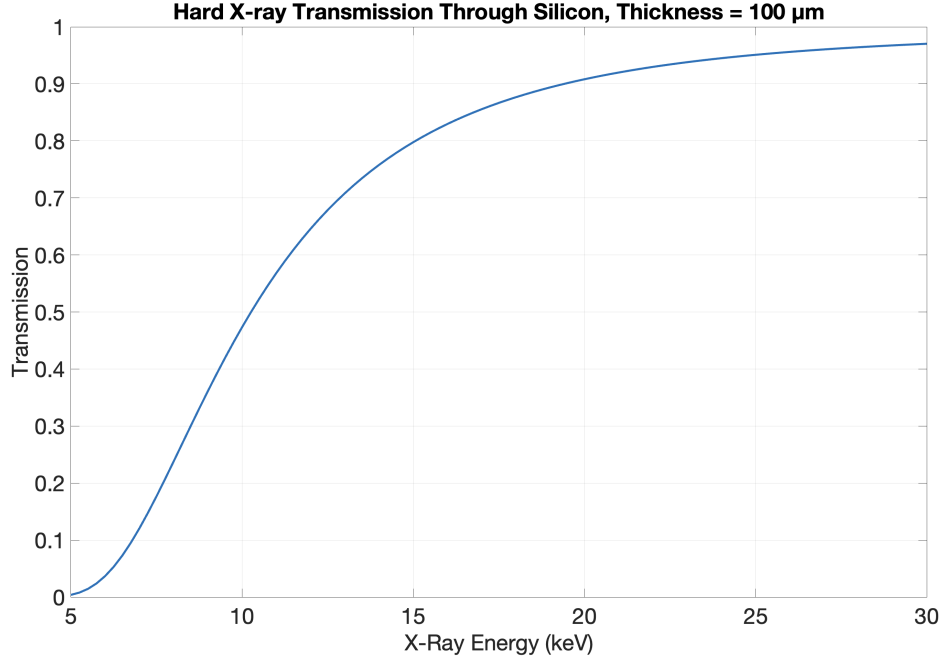


Figure 2.6: Plot of the transmission of hard X-rays with energies from 5 to 30 keV through a silicon wafer with thickness 100 μm using data from [24].

was intrinsic and undoped to mitigate any Bragg reflection interferences with doped atoms, and it was cut along the (110) crystallographic plane with a 100 mm diameter.

Because bremsstrahlung radiation is emitted with an angular distribution from the source [51], introducing a circular X-ray window through which the photons travel essentially provides us a conical radiation source similar to the ICS source at the MuCLS. If we assume that the thin-film target generates radiation from the center of the 2.75 inch cube vacuum chamber that it is held in and only exits the chamber through the circular window, then, for spectrometer design purposes, this source can be approximated as a conical radiation source with an X-ray divergence angle of 8.41° . As a result, we can utilize a silicon wafer without curvature and still achieve a corresponding 8.41° range in the angles of incidence between the photons and the planes at the crystal. As one can reasonably predict based on Figure 2.3 but will also be explicitly illustrated in simulated results later in this thesis, this angle range can yield a large spectral range, especially when probing the higher energy ranges or using small Miller indices.

Chapter 3

The Timepix3 Detector

During the 1990s, scientists from the heavy-ion program at CERN launched the WA97 experiment, a project with the objective of studying the quark-gluon plasma present during some of the earliest moments after the Big Bang. During this experiment, the need to detect trace radiation resulting from heavy-ion collisions with very fine spatial resolution led to the development of novel pixelated readout chips that could be bonded to any type of sensor (e.g. Si, GaAs) [8]. These chips, known as hybrid pixel detectors, were designed to be capable of detecting individual radiation quanta with unprecedented sensitivity and noise reduction and were characterized by an application-specific integrated circuit (ASIC) and a semiconductor sensor layer that are fabricated separately from one another and then later mated. In particular, these were a distinct advancement from monolithic pixel detectors, which were composed of a chip and sensor that were both fabricated from a single semiconductor block. Even beyond the initial scope of the WA97 experiment, these chips began finding applications in various fields such as medical imaging and radiation monitoring, which led to the inception of the Medipix collaboration between several notable institutes. With the overall success of the hybrid pixel detector project, the development of these detectors was split into two specific initiatives. One was aimed at the Medipix, a chip initially aimed at single photon counting applications in medical technology, and the other was the Timepix, a more generally

applicable detector for radiation tracking.

While various versions of both the Medipix and Timepix are available for use today, this chapter focuses on the specific detector used in our beamline, the Timepix3, and its crucial role in detecting both electrons and X-rays for this project. I first present the general structure and particle detection physics of these hybrid pixel detectors to provide the necessary context for their operation. This leads into a detailed discussion of the specific capabilities and properties of the Timepix3 chip, including how it will be integrated into our beamline, and an overview of the tools used for data collection and analysis. Finally, I briefly review other electron detection methods and compare their performance to that of the Timepix3 within the context of our beamline.

3.1 Hybrid Pixel Detector Structure

The hybrid pixel detectors are all primarily based around two main components: the sensor and the readout chip. The sensor is where an incident particle can induce a signal by creating charge carriers via interactions with atomic electrons in the depletion region of this customized semiconductor. This component is typically a reverse biased diode made of silicon, but other types of sensors based on other semiconductors like GaAs are burgeoning in popularity [8]. However, compound semiconductor sensors often encounter issues due to the abundance of charge carrier trapping centers present in these materials. Because charge carriers are vital to the signal output of the detector, these trapping centers can markedly reduce the detected energy resolution and potentially completely nullify the signal [8, 46]. The other significant component, the readout chip, is the electronics module that receives the signal from the semiconductor layer and amplifies it to relay an interpretable result to the observing physicist.

To form the pixel detector, one side of the semiconductor sensor is connected to a pixelated layer of electrodes, which is then bump-bonded via solder balls to the readout electronics

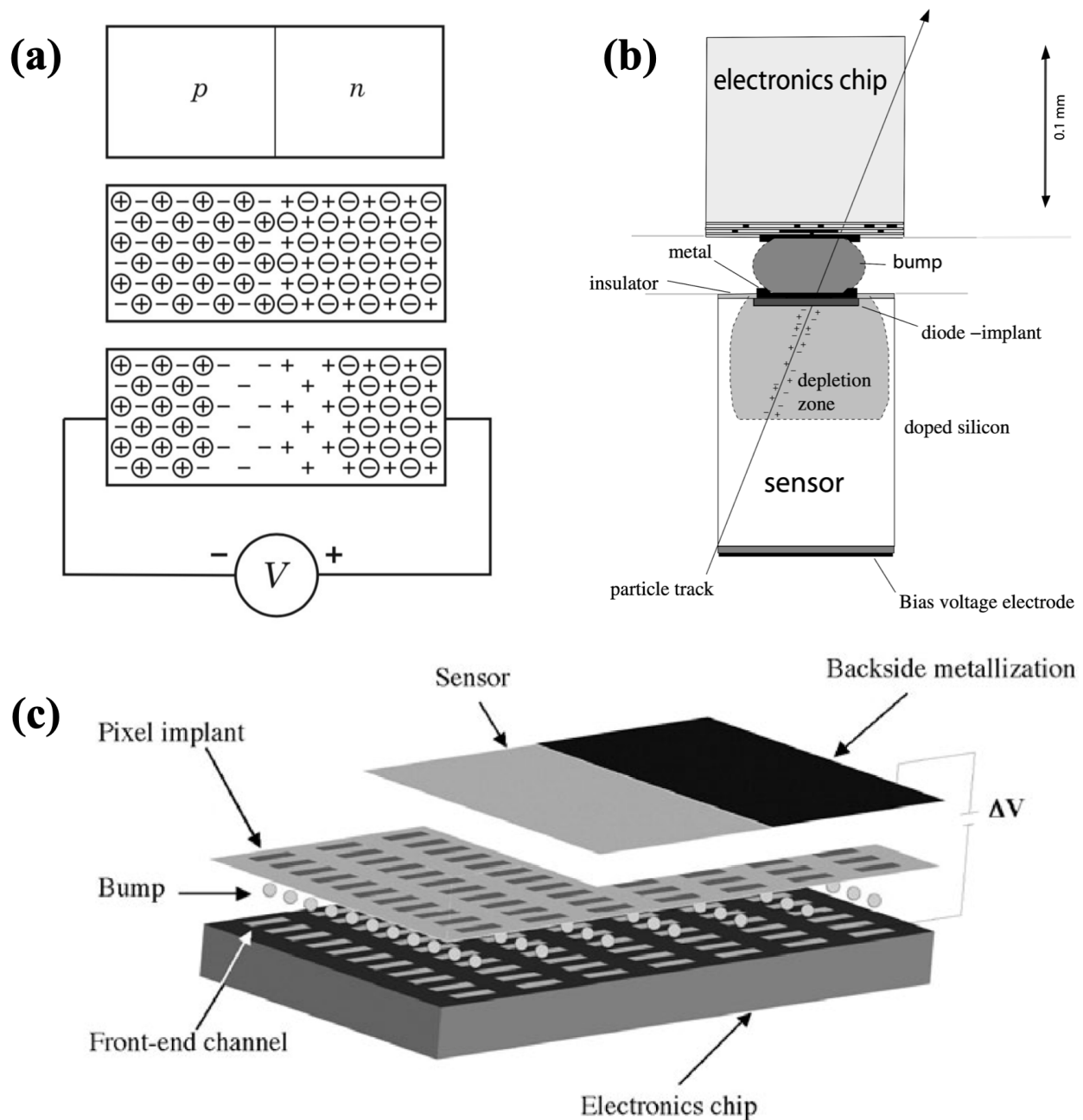


Figure 3.1: (a) Simplified diagram of a silicon sensor, which can be represented by a p-n junction with a depletion zone extended by the bias voltage [46]. (b) Diagram of a single pixel of the detector which shows how when a particle hits the silicon sensor, it creates electron-hole pairs that move toward the electronics chip bump-bonded to the sensor [44]. (c) Schematic diagram of the entire detector chip, including not only the electronics chip and the silicon sensor but also the pixel implant that underlies the pixelated detection system [44].

chip [44]. The opposite side of the semiconductor sensor is shielded by an electrode layer, known as the backside electrode, despite typically being the side that is directly in front of the incoming particles. These two layers are, thus, the electrodes across which the bias voltage for the semiconductor diode is applied. The fundamental mechanisms of a hybrid pixel detector and its individual pixels are summarized in Figure 3.1.

3.2 Particle Detection Principles

Given our group's direct interest in detecting both electrons and X-rays, the following section outlines how these particle interactions in the sensor lead to a detectable signal for both charged particles, like electrons, and neutral particles, like photons.

As charged particles pass through the sensor layer, they interact with atomic electrons via Coulomb scattering, which generates free electron-hole pairs that move to the pixelated electrode layer due to the applied bias voltage across the semiconductor [8]. Upon formation, however, these electron-hole pairs are influenced by various phenomena that affect their movement toward the electrodes. For one, a plasma effect immediately occurs following the creation of a region of high charge density, which delays their arrival at the electrode [1]. Also, a funneling effect draws the charge carriers in the center of the plasma toward the electrode layer [10]. Simultaneously, the cluster of electron-hole pairs undergo thermal diffusion and drift motion due to the electric field, which leads to spreading of these carriers into neighboring electrodes. This results in what is known as the charge sharing effect, where the signal induced by a single particle is detected across multiple neighboring pixels, and it has previously been studied in both Timepix and Medipix detector chips [10, 36]. As previously mentioned, once the charge carriers arrive at the electrode layer, they induce a voltage pulse in the electrodes, which is then amplified within the readout electronics, and this amplified signal contributes directly to the ToT measurements described later.

Unlike charged particles, neutral particles do not ionize matter along their trajectory

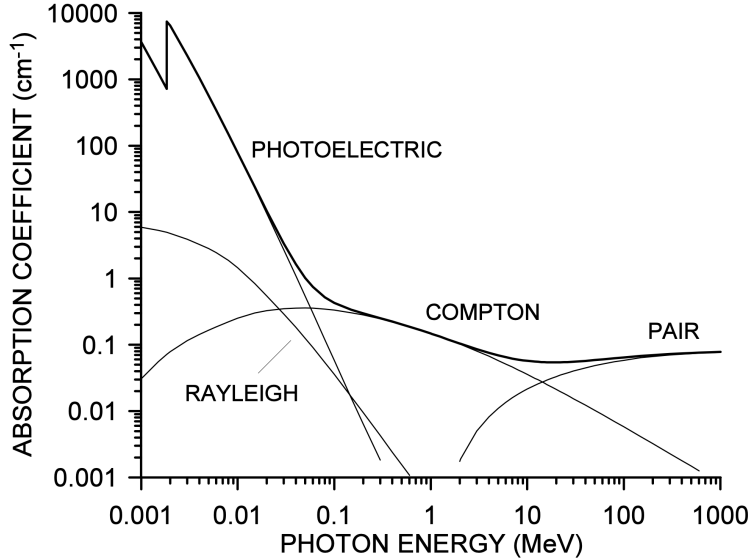


Figure 3.2: Plot depicting the photon absorption coefficient in silicon as a function of photon energy [46]. Depending on the photon energy, there are different mechanisms of absorption that are dominant. At the lower end of energies on this plot, which is our X-ray energy range of interest, it is clear that photoelectric absorption dominates.

through the semiconductor sensor layer [8]. Instead, they interact with the material through different specific processes that emit one or more charged particles which can then be detected by the electrodes in a similar manner as with the detection of charged particles. For instance, the photoelectric effect and Compton scattering are some of the most significant contributors to charge emission and, consequently, signal detection [46]. How dominant either of these processes are depends on the photon energy as depicted in Figure 3.2. Regardless, both of these processes result in the emission of an atomic electron within the semiconductor sensor layer, which leaves a track that is essentially identical to that of a detected electron. As a result, there is no observable difference between the detection of photons and electrons in the Timepix sensor, apart from a lower detective quantum efficiency with photons [8].

3.3 The Timepix3 Chip

The Timepix3 chip is a 2 cm² ASIC that is partitioned into a 256 x 256 grid of pixels with a pixel size of 55 μm, and each of these pixels is connected to its own specific readout

electronics [41]. The electronics chip is bump-bonded to a silicon sensor and wired to a PCB, which is connected to a USB interface. Thus, this chip can be connected to a computer, and, by using the proper software, we are able to control the detector and both obtain and visualize data simultaneously. The initial creation of the Timepix chips marked a distinct development for detectors because it allowed measurements of the energy deposited by the detected radiation and the timestamp of its arrival. These two measurement modes are known as ToT and ToA, respectively. The creation of the Timepix3 advanced this technology by enabling, for the first time, simultaneous usage of both modes, allowing for unprecedented versatility in its measurement capabilities [41].

ToT, or Time over Threshold, represents the time during each frame for each pixel where the input charge exceeds the comparator threshold value set by the user [48]. When an incident particle or photon generates charges in the sensor layer that is larger than the threshold, a counter in that pixel's readout electronics activates as long as the decaying signal remains above the threshold. This deposited charge is proportional to the energy of the particle or photon, and, similarly, the time for the charge to dissipate is proportional to the amount of charge. Thus, a ToT measurement during a given frame for a given pixel provides an indirect measurement of the energy incident on that pixel during that frame. Using X-ray sources of known photon energies, each pixel can be calibrated according to a function that is nonlinear for energies near the threshold but approximately linear otherwise [28, 29]:

$$\text{ToT}(E) = aE + b - \frac{c}{E - t} \quad (3.1)$$

where E is the deposited energy, (a, b, c) are calibration parameters, and t is an additional calibration parameter that represents the threshold of the pixel. With many ToT measurements for a wide range of X-ray energies, one can use a least-squares fit with the data to obtain values for the calibration parameters, obtaining a fitted curve for each pixel that resembles the curve in Figure 3.3. Although calibrating every pixel is a demanding process, alternative analysis using the shape of the spectral peaks can also be done to perform the calibrations

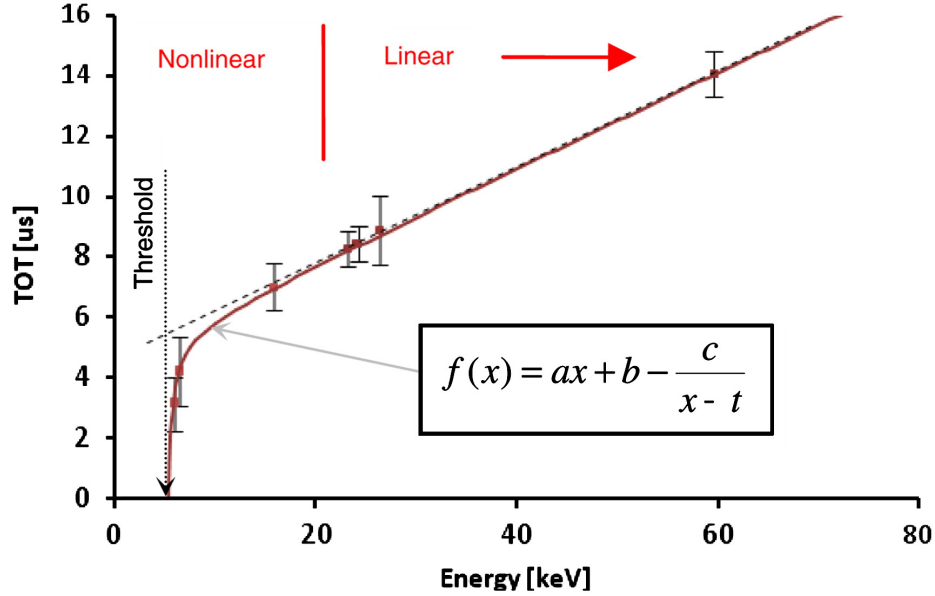


Figure 3.3: Plot of the nonlinear calibration function relating time over threshold (ToT) to particle energy for a single Timepix3 pixel [29]. Because each individual pixel possesses independent analog electronics, there effectively are 65,536 independent channels that must be calibrated using this function [28]. This dependence is modeled by equation (3.1).

with far fewer calibration points and least-squares fits [28]. This calibration for our Timepix3 detector remains a task to be completed by the next researcher working on this project.

ToA, or Time of Arrival, is a direct measurement of the time when the signal from the charges generated by the incident radiation exceeds the previously mentioned comparator threshold. The Timepix’s ASIC has a fast ToA clock that allows for time binning of 1.5625 ns (640 MHz) [41]. If we consider a 200 keV electron, for example, which travels through the Si sensor layer at relativistic speeds and, thus, at time scales that are much shorter than 1.5625 ns, this ToA clock may not appear to be fast enough for the particles and photons that will be detected. However, as this electron passes through the sensor layer, as described previously, it creates electron-hole pairs that drift towards the electrodes due to the applied bias voltage, and these drift times are much longer than 1.5625 ns [48]. In other words, ToA measurements essentially quantify how far above the readout chip the electron-hole pairs were created in the sensor layer. Thus, a combination of the ToT and ToA measurements allows precise reconstruction of information surrounding the impact of a particle or photon in the

sensor layer, including the energy of the incident radiation as well as the time of impact [48].

3.4 The Timepix3 Detector at the QLMC

For our detector, four individual Timepix3 chips were placed together to effectively create a 512 x 512 pixel detector, as in [48]. The silicon sensor layer has a thin 1 μm layer of aluminum that allows even distribution of the bias across the entire sensor layer to create an evenly sized depletion zone. As a result, the pixels across the entire chip have roughly the same responsivity except for the edge pixels because they are more exposed to electronic crosstalk and shielding effects. However, most inconsistencies between pixels are small and often manageable with proper calibration and correction techniques. The assembly of this chip configuration, the camera housing, and the SPIDR readout electronics board along with the control software, SoPhy, were made by Amsterdam Scientific Instruments (ASI) and later given to our group by researchers at the Paul Scherrer Institute (PSI) [48]. The camera and many of its key accessory components are shown in Figure 3.4.

The vacuum housing created by ASI includes interfaces for external components that are necessary for effective operation of the detector. In terms of connections to the readout electronics, there are ports for a 12V 5A power cable to power the electronics, an Ethernet cable to send commands from a computer to the detector, and a 10 Gb fiber optic cable to relay data from the detector to the computer. In addition, tubing connectors are attached to the exterior of the electronics module to connect it to a water chiller, allowing for liquid cooling to manage the detector's temperature, which can reach up to 60°C in vacuum. Because particle detection is highly sensitive to vibrations, liquid cooling is preferred for its stability and minimal disturbance. Thus, a steady flow of deionized water mixed with a few drops of glycerol is used to maintain the temperature within half a degree of room temperature, ensuring proper operation of the detector. The customized housing also includes a lead cylinder for X-ray shielding which is painted over to minimize health risks associated with

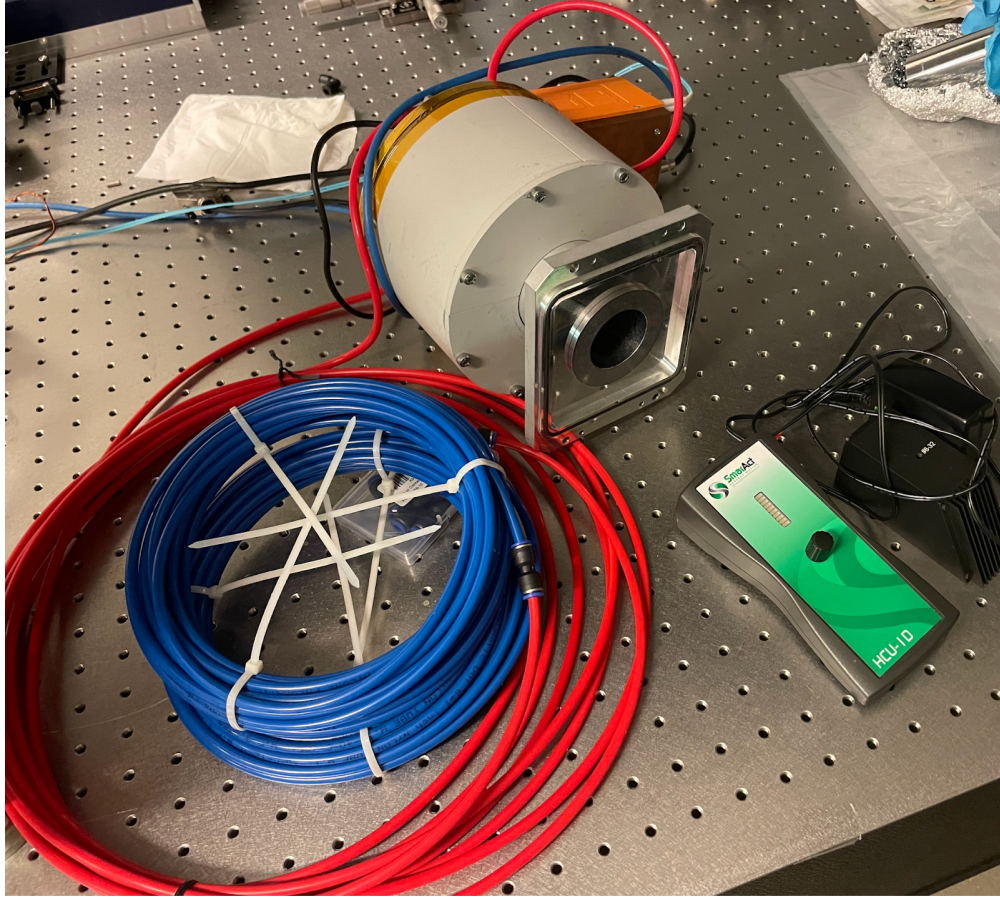


Figure 3.4: Image of our quad Timepix3 detector with its full housing connected to several important cables. The red and blue cables in the foreground are tubes that connect to the liquid chiller so that the detector's electronics board can be maintained around room temperature. The black, sky blue, and blue cables are power, fiber optic, and Ethernet cables, respectively. There is also an external SmarAct control unit visible in the right side of the image, and that is used for controlling the mechanical aluminum shutter above the detector chip.

lead exposure. There is also a mechanical shutter made of aluminum that is placed 5 mm above the silicon sensor to shield it when not in use. This shutter can be opened and closed via an external SmarAct control system.

3.5 Electron Detection using the Timepix3

As previously mentioned in the introduction, a key outcome of this overarching research branch at the QLMC is to generate and accelerate electron bunches using the DC photogun and then shape them in time and space using the focusing and steering coils and the RF compression cavity. Successful electron beam production is a crucial first step before any bremsstrahlung X-ray emission is possible in our beamline. Not only does the Timepix3 camera allow us to demonstrate and visualize the electrons generated by the DC photogun, but it also provides us with a necessary diagnostic tool for the characterization and optimization of the duration and charge level of the generated electron bunches. Furthermore, the fundamental requisite to quantum X-ray emission is shaping of electron wavepackets via electron interference, so the Timepix3 will also be instrumental to testing and measuring these waveshaping efforts.

To enable direct vacuum detection of electrons in the beamline, a conical reducer adapter was designed to connect the custom KF (Kleinflansch) flange of the Timepix3 detector with the 2.75 inch CF (ConFlat) flange standard of the beamline. This adapter was then manufactured by Xometry using a computer numerical control machine. In addition to the adapter, a support base was machined to hold the heavy lead housing of the Timepix3 detector module. Together, these external components fully integrate the camera into the beamline, as shown in Figure 3.5, and consequently allow for electron bunch measurements in vacuum.

The Timepix3 camera offers significant benefits for electron detection in our beamline, but because its proper operation requires complex setup and training, we first conducted test detections and measurements with simpler methods like a phosphor screen and a Faraday cup.

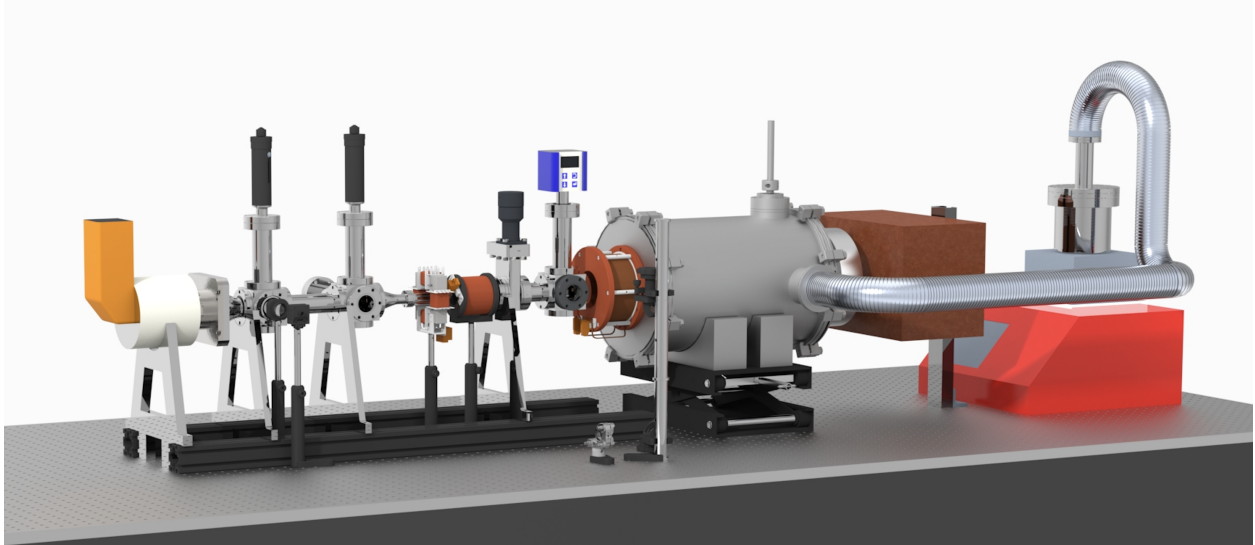


Figure 3.5: 3D rendered model of our beamline, which now has the Timepix3 detector connected to the end. This configuration will be used for electron bunch measurements.

The function of a phosphor screen is straightforward; when struck by electrons, it emits visible light that can be imaged with an optical camera [49]. As an initial benchmarking method, it is ideal for visualizing and demonstrating electron beam production. However, it offers poor spatial resolution due to light diffusion, which blurs the positions of the electron interactions. In addition, it is not very sensitive to low-energy electrons or small electron bunches, and it provides no timing information for the arrival of electrons. Similarly, a Faraday cup, which collects the charges of incident electrons and emits a measurable current proportional to the accumulated charge, is excellent for confirming beam production and estimating beam current [15]. However, it, too, lacks spatial resolution and meaningful temporal information. Thus, while both methods are valuable for their ease of implementation and simplicity in verifying beam generation, they are inadequate for our long-term goals.

The imaging capability of the Timepix3 far exceeds their abilities to precisely characterize the electron bunches generated by the DC photogun. This detector records not only the spatial distribution of the electrons with the precision of its $55\ \mu\text{m}$ pixel pitch but also provides ToA information with nanosecond precision, allowing us to accurately and precisely measure

the spatiotemporal structure of the electron bunches. Such capability is particularly important for optimizing the bunch compression and shaping process, as the time-stamped data enables high-precision analysis of bunch duration and time-dependent changes. Furthermore, simultaneously measuring the energy of incident electrons at each pixel allows for accurate knowledge of the electron energies we are able to generate. Ultimately, capturing this multi-dimensional data with the Timepix3 will yield important insights into our electron bunch dynamics, allowing us to fine-tune key parameters such as bunch length, charge uniformity, and transverse emittance. These optimizations will be essential for achieving the electron bunch characteristics necessary for well-controlled X-ray generation in subsequent stages of the experiment.

3.6 X-ray Detection using the Timepix3

Returning to the overarching X-ray spectrometer, we now discuss the significance of the Timepix3 as the detector in our design. However, the actual design and construction aspects will be left for the following chapter dedicated to that topic. Instead, this section will compare the Timepix3 to alternative detection schemes across the literature, focusing on their benefits and drawbacks and why the Timepix3 is the effective solution for our use case.

Several significant examples of X-ray spectrometers, like the ones at the LCLS and the MuCLS, use scintillator-based detection systems that rely on a scintillator screen to first convert X-ray photons into visible light [25, 43]. This scintillation light is then detected by an optical imaging system, and its intensity allows one to indirectly infer the energies of the incident X-rays. This method has several notable benefits, including high sensitivity and the ability to detect X-rays with very high energies (up to several hundred keV or more) [34]. Furthermore, scintillators can cover larger areas up to the order of several hundred or a few thousand cm^2 [35, 39], making them useful for wide-field imaging and spectroscopy. However, these advantages are outweighed by most of the disadvantages for scintillator-based detection

as far as they pertain to our lab's goals. For one, because our hard X-rays will be limited to energies around 30 keV or below, the higher-energy capabilities of scintillators is unnecessary. Furthermore, current simulations project that our X-ray beam spot sizes will never grow larger than a few cm in diameter, rendering the ability to use large-area scintillators also unnecessary. Aside from these characteristics, the Timepix3 presents unparalleled precision with timing of events, which is very difficult to achieve with scintillator-based detectors, barring the use of an ultra-precise, expensive optical camera behind the scintillator. Furthermore, scintillator-based detectors generally have relatively poor energy resolution [4] compared to the Timepix3, which will be explored in greater detail with regard to its use in the X-ray spectrometer in the next chapter. Thus, for high-resolution X-ray imaging and dynamic imaging in small, focused areas as in a synchrotron-like laboratory beamline like ours, the Timepix3 offers far more versatility and efficiency than a scintillator-based system.

Outside of scintillator-based detection schemes, other detectors, like silicon drift detectors (SDD) [37] or electron analyzers in hard X-ray photoelectron spectroscopy (HAXPES) setups [47], for example, are also utilized for various specific X-ray detection applications. However, regardless of the small specific advantages they may carry for their unique use cases, they do not offer the versatility and complex measurement ability of the Timepix3, which combines spatial, temporal, and energy information in a single system. Furthermore, the Timepix3 has event-driven time-stamping capabilities with ns-scale precision, allowing real-time tracking of photon arrival times, and the 55 μm pixel size makes it ideal for high-spatial-resolution X-ray imaging and mapping. Many of these other detection methods that might have excellent energy resolution do not provide any spatial or temporal resolution remotely as effectively as the Timepix3, making this hybrid pixel detector the superior option for our X-ray and electron detection projects that not only require energy information, but also highly precise spatially and temporally resolved data.

3.7 SoPhy Control Software

The Timepix3 detector serves two primary functions in our beamline: detecting electrons directly from the DC photogun and detecting X-ray emission from both shaped and unshaped electron bunches. These detection processes are driven by the control software, SoPhy (Software for Physics), a platform developed by ASI that facilitates data acquisition, visualization, and processing for Medipix and Timepix detectors. As complete operational instructions and interface specifics are available in the accompanying user manual [5], this section does not provide a comprehensive tutorial of the software, but rather outlines the key functionalities of SoPhy that are most relevant for operating the Timepix3 detector, specifically, and enabling both electron and X-ray detection in our beamline.

For effective communication and proper operation of the detector via SoPhy, several specific hardware requirements are necessary. As previously mentioned, the detector must be connected to the computer running SoPhy via both Ethernet and fiber optic cable, and the communication uses standard IPv4 Ethernet protocols, TCP/UDP [5]. As is the case with our current dedicated computer for SoPhy analysis, the computer connected to the detector must have the latest drivers installed and must not have any unnecessary software or a firewall that interferes with network traffic. Any issues with these items can potentially hinder effective data communication by increasing the rate of dropped packets (i.e. lost data) while communicating over UDP. To enable 10 Gb communication over the fiber optic cable, the address of the computer should be set to 192.168.100.1 with netmask 255.255.255.0, which can be set in the IPv4 Ethernet settings of the computer.

Having established the required hardware connections and settings for effective communication between SoPhy and the Timepix3 detector, we now explore the actual operation of the software, particularly focusing on the important aspects and settings of the user interface that leverage the measurement modes of the Timepix3 for electron and X-ray detection. As described earlier in this chapter, the Timepix3 revolutionized pixel detectors by allowing simultaneous ToA and ToT measurements. In addition to these two measurement modes,

SoPhy also contains a basic counting mode, which uses the electronic circuits within each pixel to record the number of detected pulses above a pre-set threshold value. In the unique “data driven” mode used by the Timepix3, all these modes can operate at the same time, allowing every pixel to simultaneously record and display the number of recorded hits, the sum of the ToT measurements of the recorded hits, and the ToA value of the latest recorded hit. During a given data acquisition period, these data can be stored for further analysis after the measurement process, and a frame-based preview can also be accessed in SoPhy during acquisition [5].

Data acquisition with the Timepix3 detector is initiated from the SoPhy main control window, which is the first window to appear after starting the software. A screenshot including labels for some of the key settings and options that are present is shown in Figure 3.6.

From this control window, a number of important actions can be taken for the detector, including selecting the proper device, setting the energy threshold value for each of the detector chips, setting the frame exposure time as well as the total number of frames to record, and starting and stopping the data acquisition. Furthermore, from this initial panel, we can swap to different panels with different purposes, like adjusting the detector settings, for example. On the two panels shown in Figure 3.7, we can access and modify various parameter settings to tailor the detection and readout process based on any specific experimental constraints. Some of these parameters are Timepix/Medipix Digital-to-Analog converters (DAC) that are settings of the actual ASIC chips and others are more general detector and readout settings. According to the scientists at the PSI, the most important DAC settings to first adjust when optimizing detected counts are IKrum, Preamp, Hist, and THL, which control the pulse shaping, the gain of the charge sensitive amplifier, the hysteresis of the discriminator, and the energy threshold of the chip, respectively.

Once data acquisition is initiated, we can open a new window to view the frames that are being recorded by clicking on “Preview” in the menu bar at the top of the window and then selecting “Medipix/Timepix frames.” This display provides the option to view either a

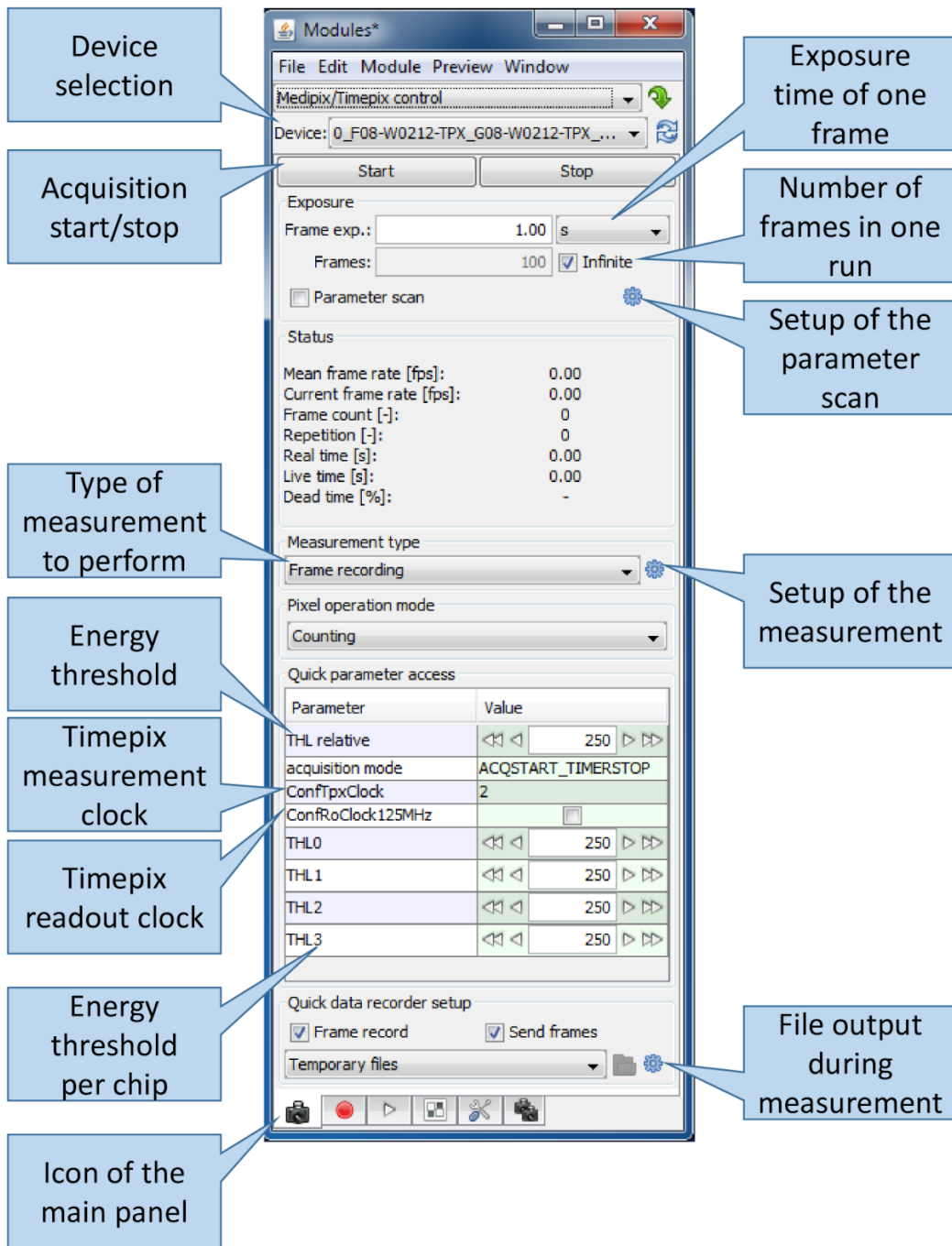


Figure 3.6: Labeled screenshot of the main control window of SoPhy [5].

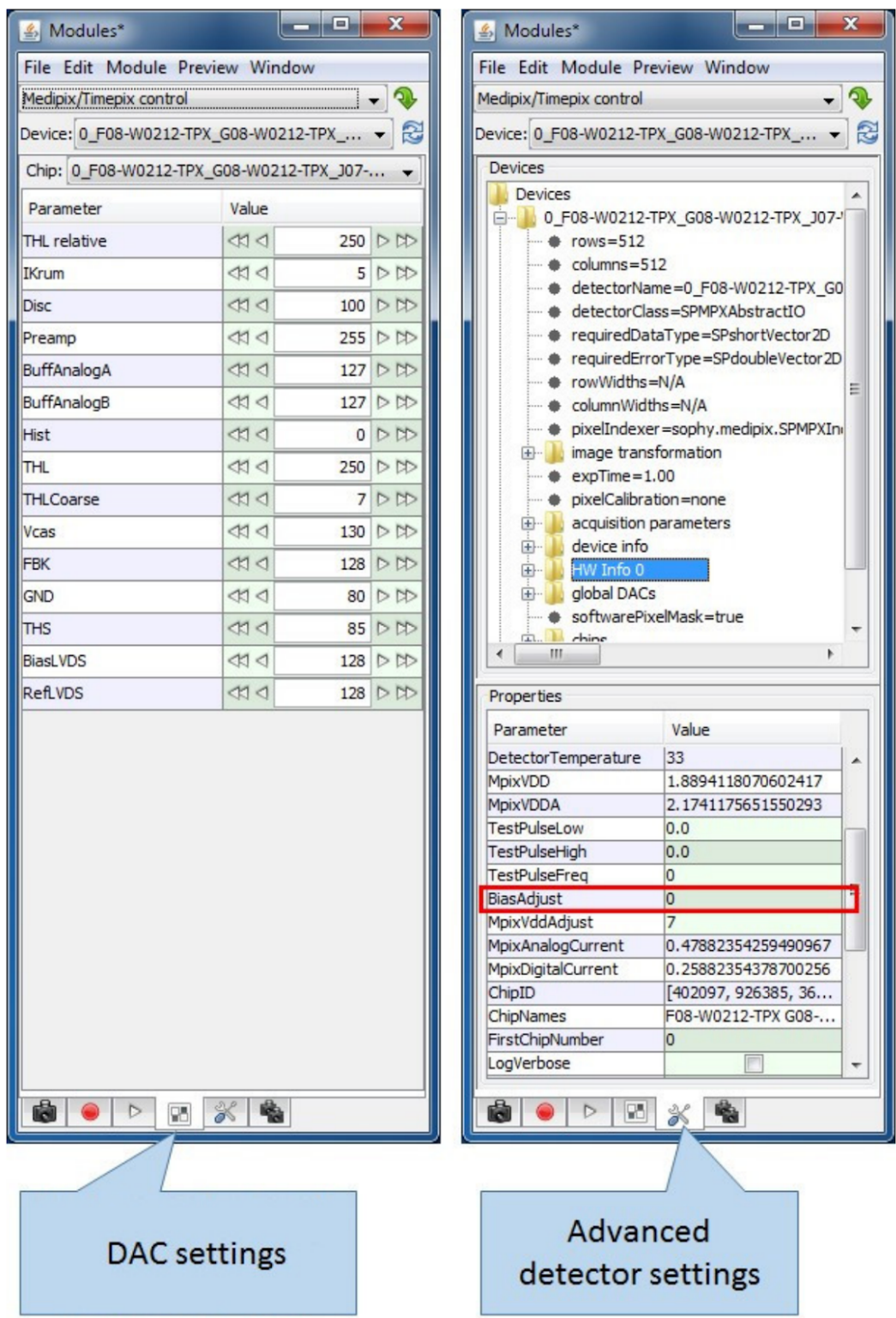


Figure 3.7: Screenshots of the DAC and advanced detector settings, where many of the most important detector parameters can be adjusted [5].

dynamic frame-by-frame image of the detection data or a cumulative image that combines all the recorded frames of the data acquisition period, both in real-time as frames are being recorded and after the acquisition has concluded. This window also allows the user to mask any hot or noisy pixels that exhibit abnormally high activity and, thus, are unreliable for accurate measurements. After the data has been acquired, screenshots and raw pixel data from this preview can be exported for further analysis as necessary.

3.8 Preliminary Measurement of Background Radiation

Using Sophy's real-time detection visualization features, we have successfully tested the Timepix3 detector with mere background radiation despite our table-top beamline still being under development. Figure 3.8 depicts a cumulative image taken by the detector over an acquisition period of 100 seconds in the default ambient conditions of our basement floor laboratory, and Figure 3.9 lists the different types of two-dimensional clusters that can be detected by the Timepix3 in response to different types of particles. As mentioned previously, photons and electrons essentially leave identical tracks which range from dots to small blobs to curly tracks, in order of increasing energy, and all three of these cluster types are clearly visible in Figure 3.8 [11]. Other clusters due to heavy ionizing particles like alpha particles and minimum ionizing particles (MIP) like cosmic rays are also visible in this image. This cluster data, combined with the energy (ToT) and timestamp (ToA) information recorded by the detector, can then be processed by pattern recognition algorithms to enable high-resolution particle detection and beamline analysis [8].

This image not only highlights the detector's sensitivity to various types of particles but also demonstrates that the complex pixel detector is fully functional and ready for experiments. In addition, this preliminary data provides a snapshot of the ambient radiation that is present in our lab environment and, thus, is useful information for future research when the beamline is fully operational.

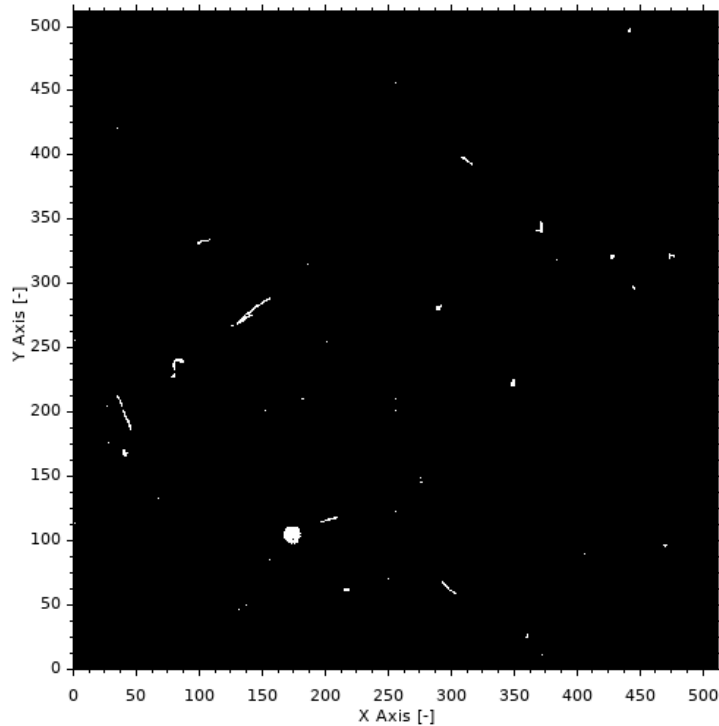


Figure 3.8: Background radiation in the lab as detected by the Timepix3 detector via SoPhy over a 100 second integration period. This measurement not only demonstrates that the Timepix3 detector is functioning as expected, but also highlights the various types of radiation (alpha particles, cosmic rays, etc.) that will always be present in the background.



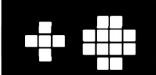
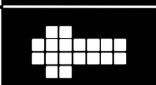

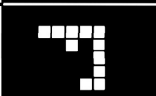
Dots		Photons and electrons
Small blobs		Photons and electrons
Heavy blobs		Heavy ionizing particles
Heavy tracks		Heavy ionizing particles → Incidence is not perpendicular to the detector's surface (Bragg curve)
Straight tracks		MIP
Curly tracks		Energetic electrons

Figure 3.9: Examples of pixel cluster patterns that are generated by different types of particles. These were defined in experiments using the Medipix2 detector, but are still detected in the same patterns in Timepix3 detectors [11].

Chapter 4

X-ray Spectrometer Design

Having presented the physical background, characteristics, and specific design of the two key components of the spectrometer, the silicon crystal diffraction grating and the Timepix3 pixel detector, we can now discuss a complete design for the HXR spectrometer that integrates these two pieces into the beamline.

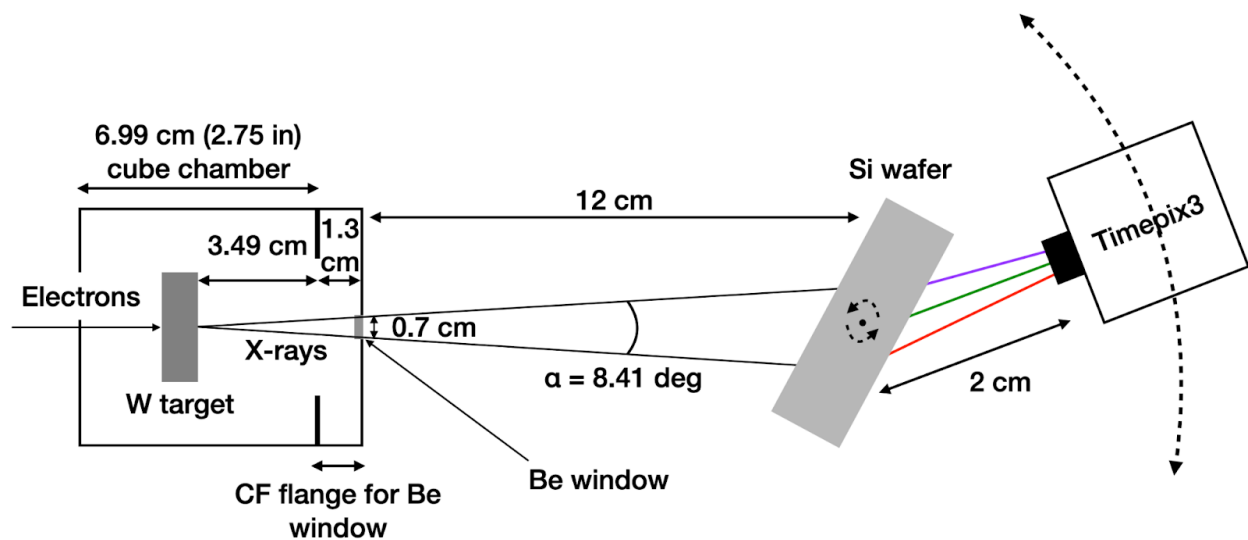


Figure 4.1: Schematic diagram (not to scale) detailing the design of our HXR spectrometer from a top-down view, including the electrons hitting the tungsten (W) target to emit bremsstrahlung radiation, which then travels out of the vacuum chamber toward the silicon crystal and then to the Timepix3 detector. Dashed lines/arrows represent crystal rotation and detector revolution to access different energy ranges and/or crystallographic planes.

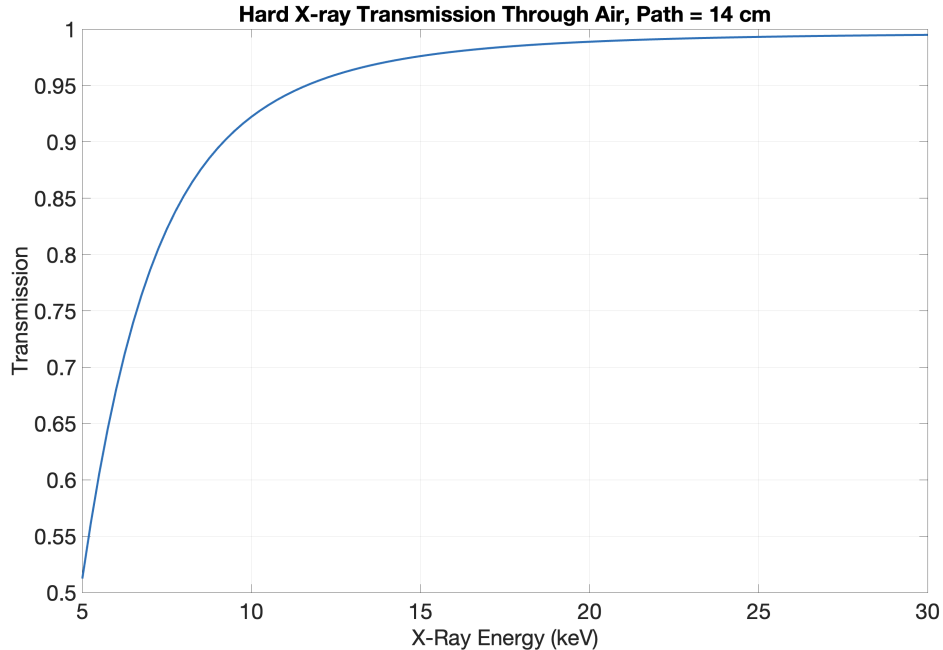


Figure 4.2: Plot of the transmission of hard X-rays with energies from 5 to 30 keV through air over a path length of 14 cm using data from [24].

Figure 4.1 depicts a labeled schematic of the spectrometer from a top-down view, starting from the generation of bremsstrahlung radiation via interactions between accelerated electron bunches, whether shaped or unshaped, and a thin-film tungsten target in vacuum. These X-rays then exit the vacuum chamber through a DuraBeryllium X-ray window from MOXTEK, inc., after which the X-rays propagate under ambient conditions in air. We will build the spectrometer outside of vacuum as transmission of hard X-rays through air is significant for most of our energy range of interest, as shown in Figure 4.2, and this approach allows us to avoid the difficulties of maintaining vacuum over a larger volume. Once the divergent X-ray beam has exited the vacuum chamber, it travels toward the silicon crystal to undergo Bragg diffraction and the resulting dispersed X-rays then reconverge toward a small spot at the Timepix3 hybrid pixel detector.

This layout also includes the dimensions of existing components of the beamline that are important for the spectrometer as well as preliminary plans for the distances between the components of the spectrometer, which will be very important for obtaining an ideal

beam spot at the detector as we will explore further later in this chapter. Another important characteristic highlighted here is the two primary degrees of freedom within the spectrometer that allow for the switching of diffraction planes and selection of photon energy ranges: rotation of the Si wafer about its axis and revolution of the Timepix3 about that same axis of the wafer, which are both represented by dashed arrows.

4.1 A Conceptual Base Case - The Silicon Monochromator

The conceptual development of the spectrometer began with a base case, whose purpose was for us to fully understand the design of a monochromator apparatus using the silicon wafer for Bragg reflection. This base case included all of the main components of the spectrometer design, including the divergent X-ray source, an X-ray window, a silicon diffraction grating, and the Timepix3 pixel detector. The primary simplification of this base case was the assumption that the X-ray window is very small and only allows the transmission of a single bremsstrahlung ray, thus only necessitating consideration of a single Bragg condition. A schematic of this setup is depicted in Figure 4.3, with labels for relevant parts and important angles.

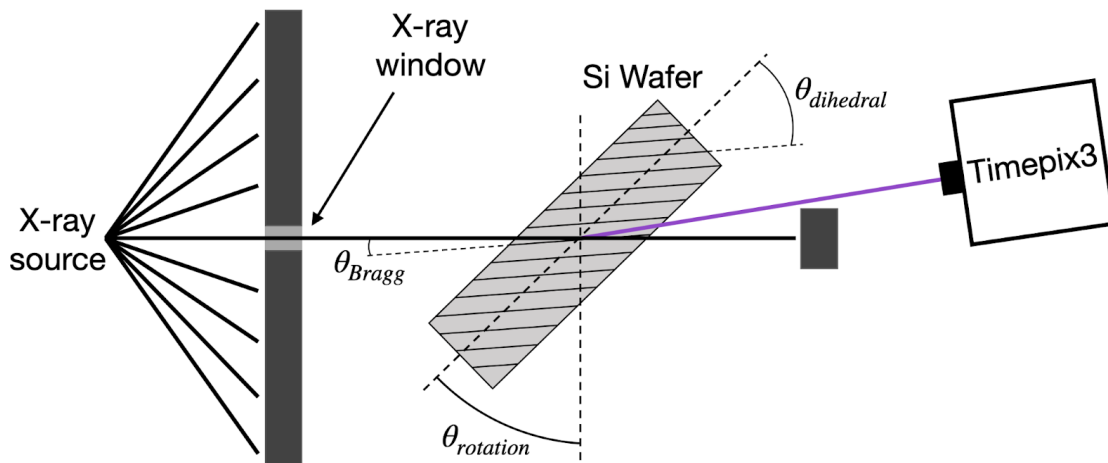


Figure 4.3: Simplified diagram of a monochromator based around the same design as our spectrometer, except relying on a single ray of photons hitting the crystal as opposed to a diverging beam. Important components and angles are labeled.

In the diagram, the dihedral angle is the angle between the Miller-indexed plane being used and the surface of the crystal, the rotation angle is the angle that the crystal has been rotated about its central axis perpendicular to the page in that diagram, and the Bragg angle is the incident angle between the incoming ray and the selected plane family. In this setup, once a crystal plane family (and, consequently, a dihedral angle) is chosen, the crystal can be selectively rotated to vary the Bragg angle. As a result, rotation of the crystal effectively allows for the selective Bragg reflection of photons with wavelength satisfying the Bragg condition for the given Bragg angle while other photons are either transmitted through the crystal or reflected in other directions by other planes. To obtain the necessary rotation angle to selectively reflect a photon with an energy corresponding to a specific Bragg angle by the Bragg equation, we apply a simple equation based on the geometry of the setup:

$$\theta_r = 90^\circ - \theta_B - \theta_d \quad (4.1)$$

Thus, for a given plane family and dihedral angle, we can increase the Bragg angle by decreasing the rotation angle, and vice versa. Figure 4.4 presents an example of how decreasing the rotation angle directly causes an increase in Bragg angle and, hence, an decrease in the energy of the photons that are reflected toward the detector by the monochromator. In this example, we have

$$\theta_{r,1} > \theta_{r,2} > \theta_{r,3} \quad (4.2)$$

which leads to Bragg reflections for incident angles that are related by

$$\theta_{B,1} < \theta_{B,2} < \theta_{B,3} \quad (4.3)$$

and, consequently, Bragg reflection of photons with energies that are related by

$$E_1 > E_2 > E_3 \quad (4.4)$$

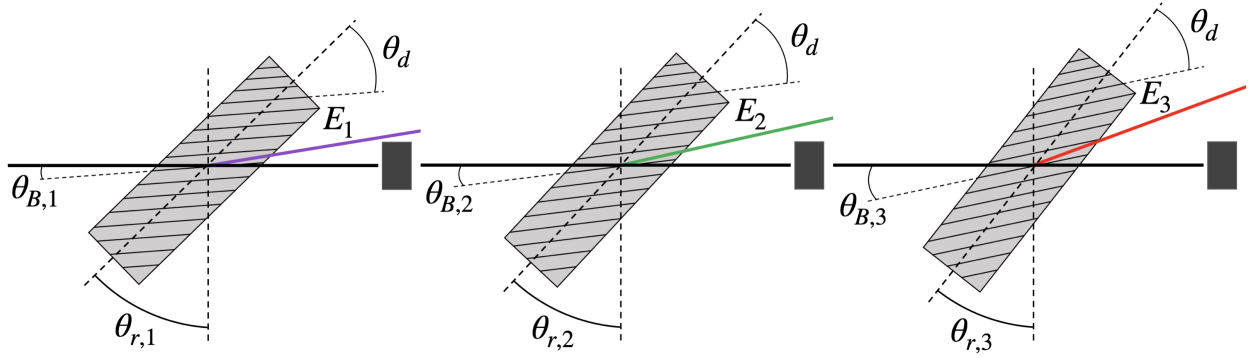


Figure 4.4: Three snapshots of the Bragg reflection interaction at the silicon crystal, each with differing crystal rotation angles and, hence, differing Bragg angles and differing selected X-ray energy (decreasing energy from left to right snapshots).

4.2 The Full X-ray Spectrometer

Now, having established and understood the geometry of the monochromator configuration, we removed the simplification of a very small X-ray window, and accounted for a conically diverging beam of X-rays propagating from the source to the silicon crystal. This setup introduces a parameter, α , which quantifies the divergence angle of the beam as seen by the silicon wafer. As the diverging beam hits the crystal, different parts of the beam scatter at different angles with respect to a given family of diffraction planes, just as in the setup at the MuCLS (visualized in Figure 2.5). This variation in Bragg angles corresponds to a variation in the photon energy that is selectively reflected from each "ray" of the incident X-rays, which effectively enables separation of the incoming X-rays into its constituent wavelengths as a function of each ray's position within the conic output. The central ray of the conic output (i.e. the ray that propagates perpendicular to the X-ray window) is used as a reference point, and it hits the selected plane at an angle, $\theta_{B,0}$, which allows selective Bragg reflection of photons from that ray with energy E_0 . Figure 4.5 introduces the conic output from the X-ray source as well as the newly defined parameters. In addition, it also presents the geometry of the setup relative to a 3-dimensional coordinate system where the central ray is propagating along the negative z-direction.

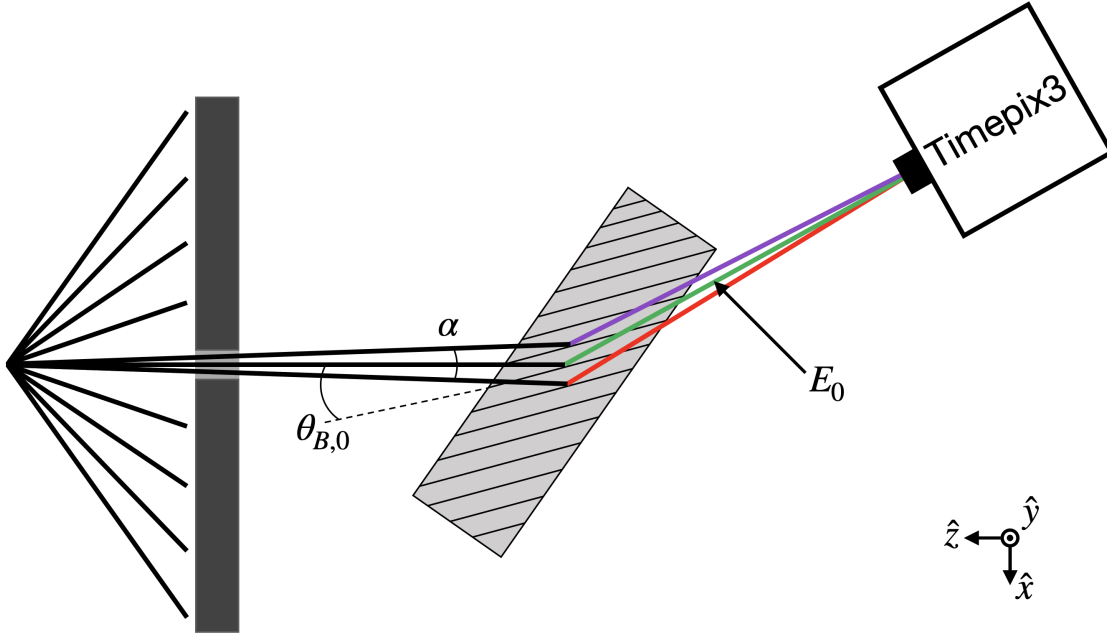


Figure 4.5: An update to Figure 4.3 to display the spectrometer setup which includes a diverging X-ray beam with divergence α and central ray energy E_0 , which corresponds to a Bragg angle of $\theta_{B,0}$.

The varying angles of incidence across the beam spot between the X-rays and the chosen crystal plane along the x -direction is very clear and follows directly from the previous monochromator examples. An additional consideration necessary to fully characterize the design of this spectrometer configuration, however, is the variation of the Bragg conditions at the crystal along the y -direction which is not intuitive from the perspective that has been shown. The diagram only provides a cross-sectional depiction of the design at $y = 0$ and highlights the variation in Bragg condition along the x -direction. To address this shortcoming, we first analyzed this design from a circular cross section of the diverging X-rays in the xy -plane, as visualized with a unique set of coordinate axes in Figure 4.6. This depiction also includes an example point within the system that corresponds to a point that is intersected by one of the infinite rays within the diverging X-ray beam.

With this cross section, we arbitrarily devised a set of coordinate axes that assigns a pair of values to every ray in the diverging beam to describe its divergence from the X-ray source in both the x - and y -directions. To further explain this idea, we take an example of a ray

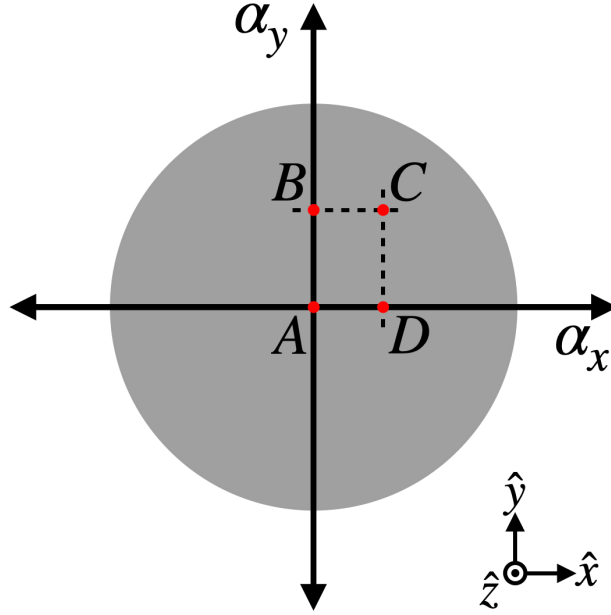


Figure 4.6: Circular cross section of the diverging X-ray beam placed in the context of a uniquely defined coordinate system that quantifies all of the beam's rays by its angular divergence from the axes in both horizontal and vertical directions. For example, the ray passing through C has α_x and α_y coordinates equal to the angle between the ray passing through A and the ray passing through D and B , respectively.

diverging from the X-ray source and passing through point C . Within this coordinate system, we can define an angle, α_x , that represents the angle between the central ray (the ray passing through point A) and the ray passing through point D , which alternatively can be described as the example ray's divergence from the source along the x -axis. By a similar token, we can define α_y as the angle between the central ray and the ray passing through point B or, in other words, the example ray's divergence from the source along the y -axis. As a result, we have successfully established a pair of values that uniquely describe the angular divergence of the ray passing through point C from the central ray. More generally, this system allows every ray within the beam to be defined by a constant coordinate pair while the beam propagates from the source to the diffraction crystal and its constituent rays diverge.

Quantifying every ray's divergence with respect to the central ray in this manner clearly demonstrates a variation in Bragg scattering angle across the beam beyond (in particular, along the y -direction) what is visualized in the 2-dimensional depiction in Figure 4.5. In fact,

the Bragg angle, θ_B , for every ray can be written as a function of $\theta_{B,0}$, α_x , and α_y according to the following elegant relation:

$$\theta_B = \arcsin [\sin (\theta_{B,0}) \cos (\alpha_y)] + \alpha_x \quad (4.5)$$

This relation can be derived by first constructing an imaginary line through the X-ray source that is perpendicular to the crystal plane family of interest. The dependence on α_x can be derived by computing the angles of right triangles with side lengths along the ray of interest, the planes, and the line we just constructed. On the other hand, the dependence on α_y can be derived by solving a few trigonometric relations involving the distances from the source to the plane along that line and along both the central ray and the ray of interest, the α_y value for the ray of interest, and the Bragg angles formed by both rays yields the desired result.

One can make the observation that different rays effectively “see” different atomic spacings along the plane that they scatter from. A helpful example to visualize this difference is to imagine an atomic lattice containing only four atoms in a square formation and an X-ray source that is placed very close to one of these atoms and centered along the square’s diagonal. It becomes immediately clear that a ray that is traveling directly along the diagonal sees a sharply different distance between the atoms it passes by than a ray that diverges 45° from the diagonal and effectively travels along the side length of the square lattice. In other words, the diagonal of the lattice is a significantly larger distance than the side length. However, this consideration does not present any additional changes to the Bragg conditions because the effective lattice spacing utilized in Bragg’s Law is merely the separation between the planes, which is not affected by the angle of incidence with the plane and the atoms that lie on it and only depends on the Miller indices of the plane. As a result, once a diffraction plane family and, consequently, an effective lattice plane spacing is selected for measurements, the only variation in the Bragg condition between different rays is due to variations in the Bragg angles.

4.3 Simulating the Energy Distribution

At this point, we have established a foundation for how the divergent X-ray beam will interact with the silicon wafer diffraction grating and how Bragg's Law governs the occurrence of these interactions as well as the appearance of the resulting spectrum. With these physics principles in mind, we were able to effectively simulate how the resulting energy distribution would look on the Timepix3 detector's pixelated screen, as well as characterize the effective resolution of each pixel or, in other words, the range of photon energies that will cause the associated X-ray to hit a given pixel.

The energy distribution simulations were computed by subdividing the circular cross section (as in Figure 4.6) of the initial diverging beam of bremsstrahlung radiation into many individual rays of photons. This was achieved by mapping a square grid of points onto the circle, with any points falling outside the circle point being removed and, thus, forming a roughly Cartesian-like arrangement of points within the beam's cross section. The grid was aligned such that it divided the diameters of the circle along the α_x - and α_y -axes into 10,000 evenly spaced points, with this number being an adjustable parameter for simulation. Then, as described in the previous section, each of these points can be associated with a unique ray with a unique α_x and α_y pair. With this in mind, the simulation then calculates the Bragg scattering of each ray onto the Timepix3 pixel detector given the knowledge of both the diffraction plane in use, the photon energy of the central ray, and the assumption that the detector is positioned such that the central ray hits the center of the detector.

Once the energy of every Bragg reflected X-ray and their positions on the detector screen have been calculated, every pixel hit by the beam is assigned a single value equivalent to the mean of the energies of all the photons that hit that pixel. The pixels hit by the beam can be identified by first understanding that the diffraction planes in our formulation are all rotated about axes that are all parallel to the y -axis. Because of this, the rays are not deflected in the y -direction at all, but rather only in the x -direction, leading to continued divergence in the y -direction and refocusing in the x -direction after interactions at the crystal. These

effects combine to yield an elliptical beam cross section at the detector screen with minor and major axes parallel to the x -axis and y -axis, respectively.

In this way, we are able to simulate the positional distribution of the Bragg diffracted X-ray energies, and this does not include any spectral data or intensity as a function of X-ray energy as this data will purely depend on the spectrum of the X-rays we are able to generate in the beamline as well as any material that is being studied by the X-rays. However, these simulations provide a useful benchmark to understand the way that the various X-ray energies are dispersed across the detector by this spectrometer configuration.

For the energy resolution calculations for each pixel, instead of computing the interactions of individual X-rays with the diffraction grating, we leveraged the natural geometry of the energy distribution resulting from the equation. Greater photon energies scatter to a further left pixel position on the detector in the x -direction, and, in the y -direction, greater energies scatter further from the center. Thus, within each pixel that contains data in the energy distribution, the maximum detectable energy is the energy of the ray that hits the bottom left (top left) corner of the pixel while the minimum is the energy of the ray that hits the top right (bottom right) corner for pixels in the bottom (top) half of the detector's screen. Then, by utilizing the α_x and α_y values for these rays to find the maximum and minimum energies that can hit a pixel, the energy range of the pixel can be calculated by:

$$\Delta E = E_{max} - E_{min}. \quad (4.6)$$

This formulation provides a straightforward method of quantifying the resolution of each pixel as the range of photon energies for which the associated X-rays hit the same pixel and essentially become indistinguishable.

The pair of plots in Figure 4.7 simulates the X-ray beam spot following diffraction with the (100) plane family and $E_0 = 10$ keV and distances between the spectrometer components as labeled in Figure 4.1. This simulated spectrum is a useful example to demonstrate the large spectral range that can be covered in one measurement when using smaller Miller indices

as we can probe nearly our entire photon energy range of interest, from ~ 6.12 keV to ~ 27.8 keV. It is also worth noting that while the Bragg angle (and photon energy) certainly varies as a function of y -position as described by equation 4.5, this dependence ultimately does not yield significant variation (e.g. ~ 50 eV difference between the photon energies at the bottom and the center of the beam spot) in our simulated results because the change in α_y across the X-ray spot is only on the order of a few degrees.

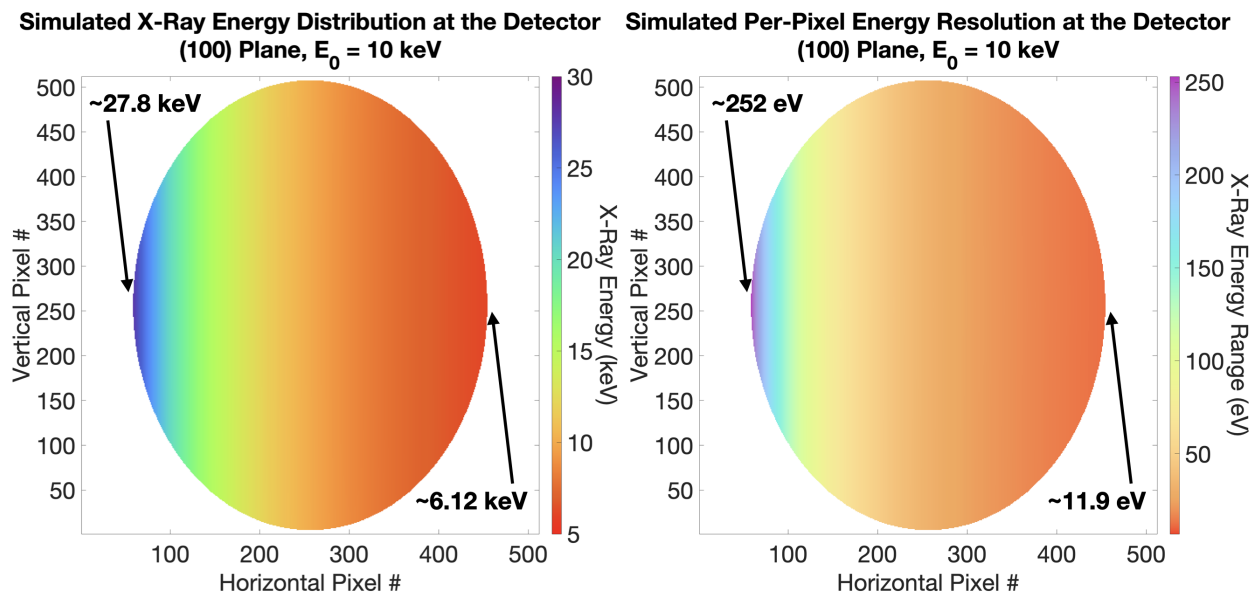


Figure 4.7: Simulated plots visualizing the X-ray energy distribution and per-pixel energy resolution at the detector as dispersed by the (100) plane with central ray energy 10 keV. The color bar is meant to be similar to the colors of the visible wavelength range, which range from red (low photon energy) to violet (high photon energy), to visualize the varying X-ray energies, although X-rays are not actually physically visible in colors we can perceive.

Another interesting characteristic of Bragg reflection that is highlighted in these simulated data is the nonlinear relationship between Bragg angle and the energy of the reflected X-ray, which was previously illustrated in Figure 2.3. These simulated plots allow us to clearly observe how at larger photon energies, small changes in the Bragg angle correspond to much greater changes in photon energy compared to when probing smaller photon energies. This concept is further underscored by the energy resolution plot in Figure 4.7, showing much larger changes in the photon energy from pixel to pixel for the higher energy X-rays near the

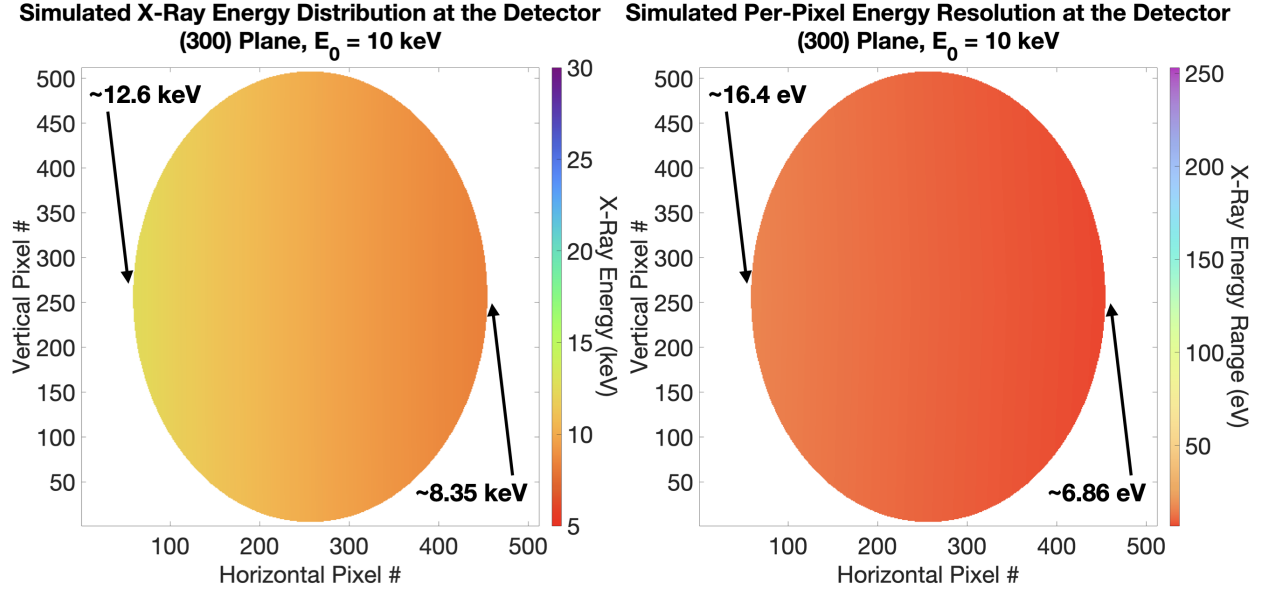


Figure 4.8: Simulated plots visualizing the X-ray energy distribution and per-pixel energy resolution at the detector as dispersed by the (300) plane with central ray energy 10 keV.

left of the beam spot compared to the pixels hit by lower energy X-rays near the right of the beam spot.

This wide range of energy resolutions for different pixels across the detector when measuring nearly the entire energy range of interest raises the question of how we can increase the resolution of our measurements and potentially probe smaller sub-ranges of photon energies. Recall that using planes with greater Miller indices can enable higher resolution measurements, so we simulated precisely how this might look.

Figure 4.8 shows the results of measuring the spectrum resulting from using the same central energy of $E_0 = 10$ keV as before, but with the (300) plane. Immediately, we observe a significantly smaller range of photon energies that is captured in the beam spot which is still spread over the same pixels as in the previous simulation. This leads to a greater energy resolution per pixel or, in other words, a smaller energy range that hits each pixel; in specific, the pixels near the left side of the spot can resolve $\sim 0.13\%$ differences in photon energies from pixel to pixel, while pixels near the right side of the spot can resolve differences as small as $\sim 0.08\%$.

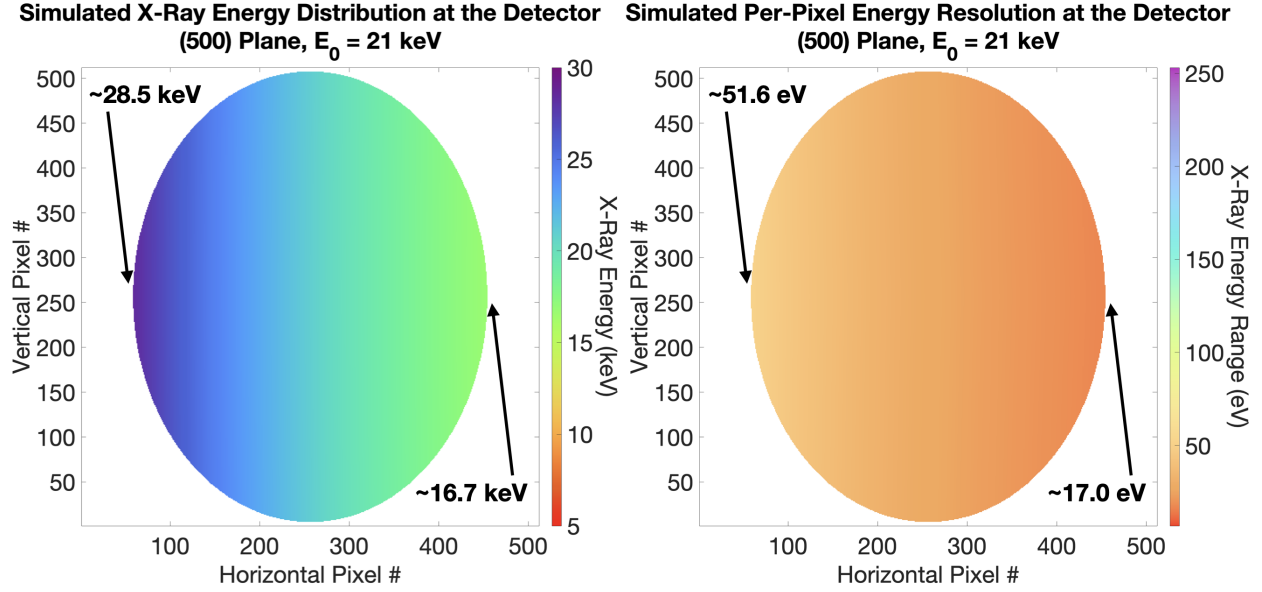


Figure 4.9: Simulated plots visualizing the X-ray energy distribution and per-pixel energy resolution at the detector as dispersed by the (500) plane with central ray energy 21 keV.

Through the use of higher Miller indices, we can similarly zoom in on higher photon energy ranges and more closely examine the energy distribution that seems so densely packed toward the left of the spot in Figure 4.7. Figure 4.9 depicts simulations using the (500) plane and a central ray energy of 21 keV. The energy resolution distribution across the pixels here clearly demonstrates the higher resolution we are able to achieve at this photon energy range as opposed to the earlier spectrum over the wider energy range. The color scale of the visualization is a clear demonstration of this fact, but taking a closer look at the actual energy ranges of each pixel, we can see the largest energy range values (lowest resolution) near the left of the beam spot are around 80% smaller than the energy ranges in that region from the spectrum over the large photon energy range. With the increased resolution, each pixel is able to capture energy ranges as small as 0.10% to 0.18% of the photon energies being measured.

Figure 4.10 displays the results of simulating with the same central ray energy (21 keV) but using the (800) plane, instead, as that is the crystal plane used for the highest photon energies in the HXR spectrometer at the LCLS [43]. As expected, we are able to decrease

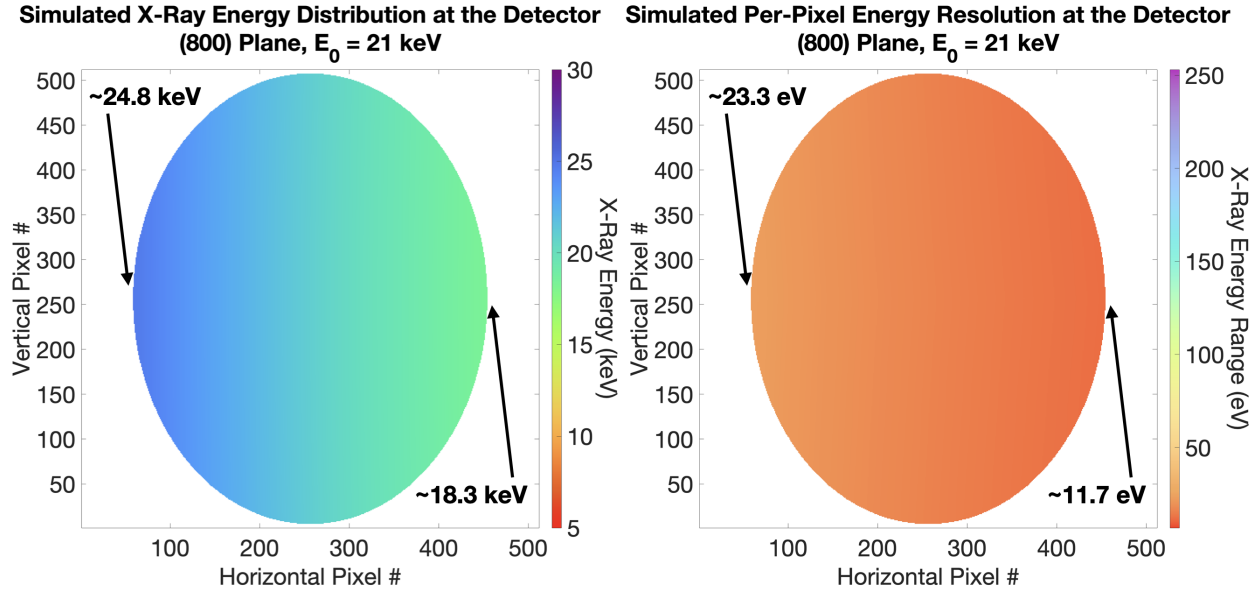


Figure 4.10: Simulated plots visualizing the X-ray energy distribution and per-pixel energy resolution at the detector as dispersed by the (800) plane with central ray energy 21 keV.

the spectral range even further by a factor of almost 2 and increase the energy resolution of our measurements with captured energy ranges per pixel from 0.06% to 0.09% of the photon energies being measured. However, it is important to note that reflections from planes with higher Miller indices can result in less intense reflections which may limit their usefulness for the purpose of a spectrometer. This reduced intensity is due to a multitude of factors, including the fact that the shorter distance between planes increases the scattering angle which can decrease reflection intensity [31]. Testing the spectrometer with different diffraction planes with both small and large Miller indices over various spectral ranges will likely be an important task in the future to determine with greater precision which planes to use for what experiments.

An alternative method of increasing the resolution while keeping the energy range of the spectrum constant is to maximize horizontal pixel usage. In this simulation, we chose the same plane and central ray energy as the first example, but we increased the distance from the X-ray source to the silicon crystal, from 12 cm to 16 cm, allowing the beam to diverge and produce a larger beam spot at the detector. This allows us to spread the spectrum

of photon energies over a greater number of pixels, resulting in greater resolution, ranging from $\sim 0.15\%$ for lower energies to $\sim 0.71\%$ for higher energies, as shown in Figure 4.11. Due to the geometry of the spectrometer setup, the greatest changes in Bragg angle and X-ray energy can be observed along the horizontal pixels, while changes across the vertical pixels are smaller by multiple orders of magnitude. As a result, maximizing the beam spot's spread across the horizontal pixels can be useful for optimizing energy resolution across the whole spectrum.

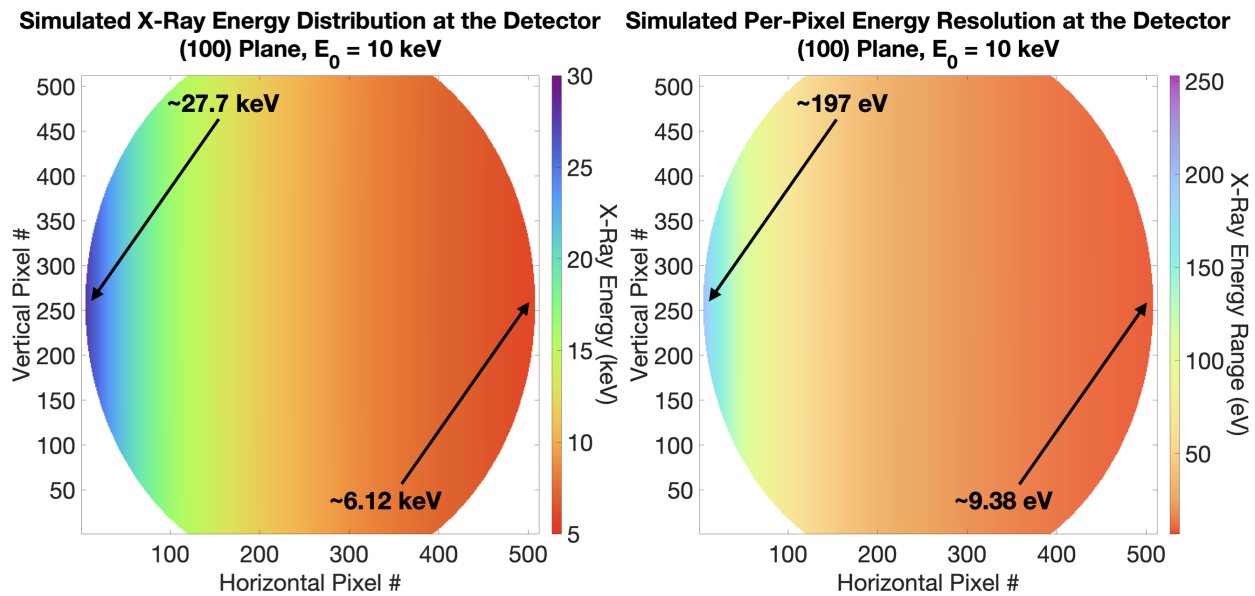


Figure 4.11: Simulated plots visualizing the X-ray energy distribution and per-pixel energy resolution at the detector as dispersed by the (100) plane with central ray energy 10 keV, but this time with a 16 cm distance between the X-ray source and the silicon crystal as opposed to 12 cm.

However, this spectrometer configuration results in some of the upper and lower regions of the beam spot being cut off at the edges of the detector screen. This occurs due to the beam continuing to diverge in the y -direction following Bragg diffraction at the crystal while beginning to converge in the x -direction due to the geometry of the diffraction planes. Thus, if we place the detector at any reasonable distance away from the silicon crystal (2 cm in this simulation), the vertical axis of the spot will be noticeably larger than the horizontal axis. To initially test and benchmark the capabilities of the spectrometer, this does not

cause immediate concern, as we will be able to observe whether Bragg diffraction is occurring as expected by the data presented along the horizontal pixels. In addition, for a diverging beam that is perfectly uniform in photon energy composition, this measurement may still prove useful as full spectral information of part of the beam will necessarily provide full spectral information of the entire uniform beam. Nonetheless, for experiments that involve, for example, characterizing the directionality and angular profile of bremsstrahlung generated by shaped electron wavepackets, obtaining spectral data across all angles of emission will likely be of utmost importance, so this method of energy resolution optimization may not be the most appropriate for these types of applications.

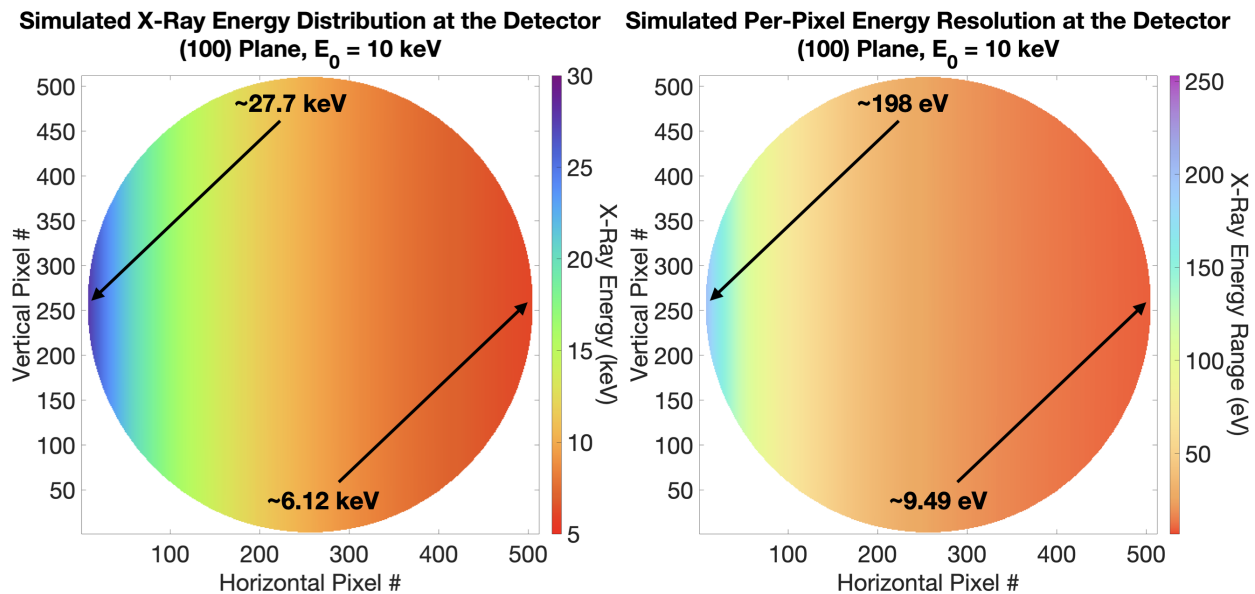


Figure 4.12: Simulated plots visualizing the X-ray energy distribution and per-pixel energy resolution at the detector as dispersed by the (100) plane with central ray energy 10 keV, but this time with a 14 cm distance between the X-ray source and the silicon crystal as opposed to 12 cm as well as a 2 mm distance between the crystal and the detector as opposed to 2 cm.

On the other hand, the simulations in Figure 4.12 depict a beam that nearly maximizes usage of horizontal pixels while still fitting the entire beam spot within the detector screen. This simulation utilized a distance of 14 cm from the X-ray source to the silicon crystal while also adjusting the distance from the crystal to the detector screen from 2 cm to 2 mm.

Evidently, this configuration not only achieves greater energy resolution by utilizing as much of the horizontal pixel range as possible but also enables spectral analysis of the edges of the beam that were cut off in the previous example. However, the very short distance required between the silicon crystal and the detector screen to minimize divergence along the y -axis may hinder such a configuration from being realistically feasible. Thus, one of the many important decisions for future researchers who construct and use this spectrometer will be to decide what distances are optimal for the specific experiments that are being conducted.

The Timepix3 detector, itself, offers a rather mediocre indirect energy resolution of around 1-2 keV through ToT measurements, which would be a detriment for a precise and useful HXR spectrometer. And yet, simulations clearly demonstrate the capability of this spectrometer design to surpass that mark by at least an order of magnitude. In fact, the energy resolution presented in the simulations above are very different from the energy resolution of the ToT measurements of a Timepix3 pixel. The energy resolutions that are calculated in the previous simulations are still achievable because within this spectrometer configuration, pixel positions act as an indirect tool for precisely measuring photon energy. The simulations will allow us to map pixel positions to photon energies at a theoretical level, and subsequent calibration using the K-edges of transition metal filters will refine this map, enabling ultrafine energy resolution even without ultrafine resolution in the Timepix3's ToT measurements.

4.4 X-ray Spectrometer Calibration

While this thesis describes a comprehensive overview of the design of our HXR spectrometer up to its construction, the accuracy of its functional operation in our beamline requires understanding and correcting for the geometric imperfections and other structural errors that may induce measured deviations from simulated spectra. This process will involve a thorough photon energy calibration of the spectrometer and will account for imperfections in wafer cuts, crystal concentricity, and detector alignment, among other characteristics. Transition

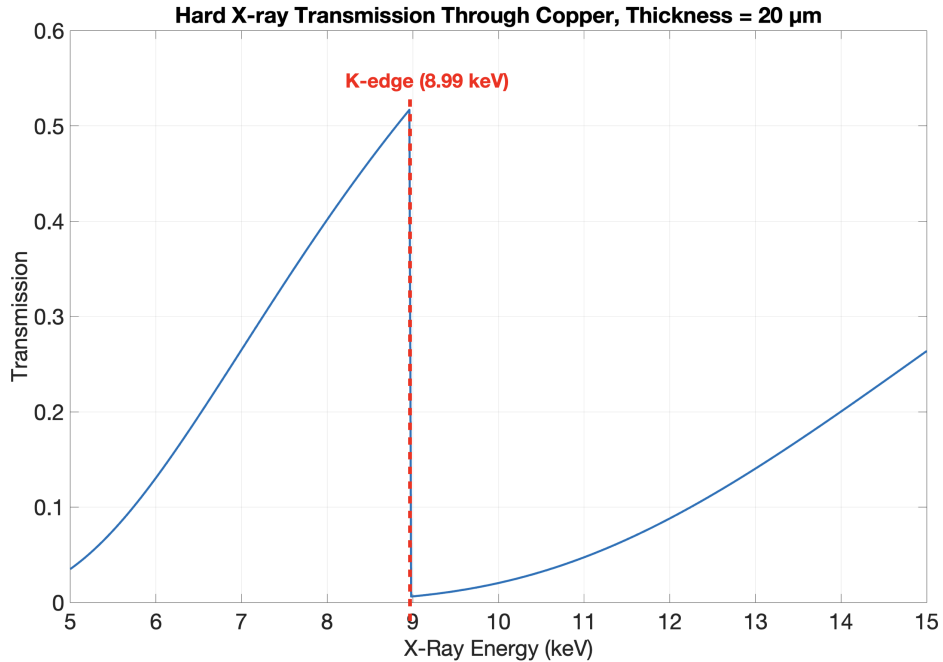


Figure 4.13: Plot of the transmission of hard X-rays with energies from 5 to 30 keV through a copper foil with thickness 20 μm using data from [24].

metal K-edges present a straightforward solution with their well-characterized, sharp spectral features that are ideal for these calibrations, offering the necessary accuracy and precision to fine-tune the spectrometer’s performance [43].

The K-edge is a sharp increase in X-ray absorption (and, consequently, a sharp decrease in transmission) by a material when the photon energy slightly exceeds the binding energy of the innermost electron shell, also known as the K-shell, of the material’s atoms [16]. For instance, copper has a K-edge at 8.99 keV, and Figure 4.13 depicts a plot of X-ray transmission through a copper foil as a function of photon energy, with a clear drop in transmission at the K-edge. Many transition metals, like copper, have K-edges that are well within the target energy range of our spectrometer, making them ideal candidates for the calibration process. Previously, researchers at the LCLS have used the K-edges of iron (7.11 keV), nickel (8.33 keV), and copper (8.99 keV) foils to calibrate their HXR spectrometer, which was designed to operate from 4 keV up to 19.5 keV [43]. In our case, where we plan to generate X-rays with energies up to 30 keV, we aim to use similar foils, including iron and copper, along with the

addition of indium foil, which has a K-edge (27.9 keV) near the top of our planned range and is commercially available. Once the spectrometer is fully constructed, we plan to conduct multiple test measurements and capture different spectra, each using a different foil placed in front of the detector. Due to the narrow absorption of X-rays with energies near the K-edge, we expect to observe distinct drops in intensity in specific regions of the measured spectra that directly correspond to the K-edge energy of the foil in use. By using various transition metal foils, we can then acquire multiple calibration points for the spectrometer across the entire energy range of the generated X-rays.

4.5 Items to Purchase

This chapter has presented the utilization of both Bragg diffraction physics with a silicon wafer and the Timepix3 pixel detector to design a HXR spectrometer for our beamline. While this design plan overviews and theoretically quantifies the key concepts and details about the spectrometer's operation, full construction and calibration will require the purchase and setup of additional items, which this section covers in detail.

The first of these items is a new dedicated computer or laptop for data collection via SoPhy. We currently have a computer provided to us by the previous team of researchers that used the Timepix3 detector and SoPhy runs well on that computer without any issues. However, we have been unable to connect to the Internet despite trying various methods like using an Ethernet cable. An online connection would be significant for potentially enabling remote data collection, especially with potential X-ray radiation risks, and also for facilitating communication with other devices to transfer any data that is collected, to name a few examples. This new computer would need to include a port for an Ethernet cable connection as well as a port for a fiber optic cable connection capable of 10 Gb data transfer to properly run experiments using the Timepix3 and SoPhy.

Also necessary are components that will hold the silicon crystal and the detector when

the spectrometer is assembled. Specifically, the spectrometer will need a rotation stage as well as a holder for the silicon crystal to rotate it and effectively switch either the diffraction planes, the central ray Bragg angle, or both. Further considerations regarding the rotational resolution that is necessary will guide purchase decisions for this component. The detector will also need a holder and a stage that can be relatively easily revolved about the crystal to allow for spectral measurements wherever the Bragg reflected beam is scattered toward. A custom-fabricated half cylindrical holder atop a positional stage would be ideal with a very thin layer of rubber to prevent sliding and rubbing during movement as well as a leather band to clamp the detector down.

Lastly, transition metal foils must be acquired for spectrometer calibration as described previously. The sharp K-edges of these metals will allow for precise calibration for X-ray energy analysis using the pixelated spectral measurements of the HXR spectrometer.

Chapter 5

Outlook and Future Plans

5.1 Summary

Ultrafast X-ray science has grown immensely from its earliest developments at large synchrotron facilities to more recent efforts studying advanced table-top laser technology in the X-ray wavelength range. Regardless of the physical scale, however, its significant potential for interdisciplinary scientific application has made it a promising branch of research with great allure. Coupling the individual advantages of both X-ray measurements and ultrafast science to ultimately probe matter at the shortest spatial and temporal scales has brought forth the potential to revolutionize our understanding of the functional properties of matter. With these promising objectives in mind, the QLMC has sought to conduct groundbreaking research in this field with both electrons and X-rays.

In this thesis, I outlined the QLMC's efforts toward building a table-top ultrafast beamline for electron and X-ray studies, including details of the DC electron gun, electron bunch shaping mechanisms, and plans to study coherent multi-state bremsstrahlung generation. I also discussed the complexity and sophisticated nature of the Timepix3 pixel detector along with an explanation of its integration into our beamline and how data collection works using the SoPhy software.

Most significantly, I detailed a comprehensive design for a hard X-ray spectrometer stationed at the end of our beamline utilizing a silicon wafer diffraction grating and the Timepix3 detector. This design process covered the fundamental physics that underlie Bragg diffraction and spectrometer gratings and how they contribute to an energy-dispersive setup for hard X-rays, the operating principles behind the Timepix3 detector and how they enable precise electron and X-ray detection in our beamline, and an in-depth analysis of how both of these two base components will be arranged to form a precise HXR spectrometer. Simulations have also demonstrated the ability for this spectrometer design to cover up to nearly 100% of the photon energy range of interest from 5 to 30 keV in a single spectrum measurement, while also having the ability to probe narrower energy ranges with less than 0.1% energy resolution.

5.2 Future Work

As noted in multiple instances throughout this thesis, there are many areas within this project where steps for future work and improvement are clearly motivated. Here, I organize these planned tasks into a single section for final review as well as future reference.

First, there remain a few items to be purchased before spectrometer construction and setup is complete and ready for X-ray spectroscopy. A new dedicated computer or laptop for the SoPhy will need to be purchased with the ability to connect and interface with the detector as well as connect to the Internet. In addition, stages and holders for both the silicon wafer and the Timepix3 detector must either be purchased or manufactured so that the spectrometer components can be precisely positioned on the optical table at the end of our beamline. Another important purchase for initial spectrometer testing will be foils made of iron, copper, and indium to calibrate the spectrometer using their sharp X-ray absorption edges. Once all of these components are prepared, the spectrometer can be assembled according to the design presented in this thesis and initial testing can begin.

Outside of spectrometer-specific work, once the beamline is properly set up and ready to detect electron bunches using the Timepix3, the team will need to run several tests to first calibrate and optimize the detector's settings. As mentioned in the Timepix3 chapter, each pixel's ToT measurements can be individually calibrated. This calibration will be vital to accurate measurements of the energy of detected electrons or photons, depending on the specific experiment. Furthermore, additional testing will be necessary to identify optimal DAC settings for our specific beamline and experimental plans.

Another element of future work will be to ensure lab safety by properly utilizing radiation shielding and testing for any stray radiation. This process will also necessitate radiation safety training for all researchers who are involved.

5.3 Outlook

The primary direct impact of this HXR spectrometer project will naturally be its ability to measure spectral information about the X-rays that are generated from our laboratory table-top beamline. This capability will be crucial for many different experiments in the future, ranging from multi-state radiation studies to potential X-ray spectroscopy experiments. As briefly discussed earlier, the former is one of the experimental projects that will be explored in the near future at the QLMC and the HXR spectrometer will be the key to measuring both unshaped and shaped-electron X-ray emission. In addition, by taking many spectral measurements, researchers will be able to fully characterize the generated radiation, effectively measuring the angular dependence of photon energy in the X-ray emission and experimentally examining the theoretical predictions of [51] as displayed in Figure 1.5. This project has the potential to unveil new frontiers of research with the novel demonstration of spatial and spectral control over atomic bremsstrahlung emission via shaping of input electron wavepackets. For example, modern quantum information theory has shown that quantum system transitions can be driven by optical frequency modulation of electron beams, which

will directly stem from the QED studies conducted in this project.

The HXR spectrometer's vital role in these experiments analyzing multi-state X-ray radiation will also be fundamental for future applications made possible by this innovative science. These applications include QED-based ultracompact and portable X-ray devices that can substantially augment security measures to detect high-risk weapons or other equipment in military operations and commercial airports, for example. In medical settings, this technology could enhance X-ray imaging procedures by providing greater resolution as well as minimizing radiation exposure to patients, improving the efficiency of tests and diagnoses for various internal health conditions. Regardless of the specific application, this future technology offers the potential of a new era in X-ray science, with devices that require far less cost and can be readily mass produced. It also presents the potential for full integrability into photonic chip systems, which, in turn, enables the production of entangled distributed quantum networks of on-chip X-ray systems built for diverse environment spectroscopy characterization, for example. The vast application space of these ultracompact and portable devices not only highlights the profound potential this research carries for a future of sustainably scalable X-ray technology but also presents this technology as a transformative force that will redefine standards in industries from healthcare to national security and beyond.

Bibliography

- [1] A. Alberigi Quaranta, A. Taroni, and G. Zanarini. Plasma time and related delay effects in solid state detectors. *Nuclear Instruments and Methods*, 72(1):72–76, 1969.
- [2] Enrico Allaria, L Badano, S Bassanese, Flavio Capotondi, D Castronovo, Paolo Cinquegrana, MB Danailov, G D’auria, A Demidovich, R De Monte, et al. The fermi free-electron lasers. *Journal of synchrotron radiation*, 22(3):485–491, 2015.
- [3] Massimo Altarelli, Reinhard Brinkmann, and Majed Chergui. The european x-ray free-electron laser. technical design report. 2007.
- [4] Khalil Amgarou and Margarita Herranz. State-of-the-art and challenges of non-destructive techniques for in-situ radiological characterization of nuclear facilities to be dismantled. *Nuclear Engineering and Technology*, 53(11):3491–3504, 2021.
- [5] Amsterdam Scientific Instruments, Amsterdam, Netherlands. *SoPhy Software for Physics: Timepix and Timepix3 User Manual*, September 2018.
- [6] Valeri Ayvazyan, Nicoleta Baboi, J Bähr, Vladimir Balandin, Bolko Beutner, A Brandt, I Bohnet, A Boltzmann, Reinhard Brinkmann, OI Brovko, et al. First operation of a free-electron laser generating gw power radiation at 32 nm wavelength. *The European Physical Journal D-Atomic, Molecular, Optical and Plasma Physics*, 37:297–303, 2006.
- [7] Andrea Bellandi, Julien Branlard, Jorge Diaz Cruz, Sebastian Aderhold, Andrew Benwell, Axel Brachmann, Sonya Hoobler, Alessandro Ratti, Dan Gonnella, Janice Nelson,

- Ryan Douglas Porter, and Lisa Zacarias. Narrow bandwidth active noise control for microphonics rejection in superconducting cavities at lcls-ii, 2022.
- [8] Thomas Billoud. *Characterization of the radiation field in ATLAS using Timepix detectors*. PhD thesis, Czech Technical University in Prague (CZ), 2019.
- [9] Christoph Bostedt, Sébastien Boutet, David M. Fritz, Zhirong Huang, Hae Ja Lee, Henrik T. Lemke, Aymeric Robert, William F. Schlotter, Joshua J. Turner, and Garth J. Williams. Linac coherent light source: The first five years. *Rev. Mod. Phys.*, 88:015007, Mar 2016.
- [10] J. Bouchami, Andrea Gutierrez, A. Houdayer, J. Idarraga, Jan Jakubek, C. Lebel, Claude Leroy, Jean-Pierre Martin, M. Platkevic, and Stanislav Pospisil. Study of the charge sharing in silicon pixel detector with heavy ionizing particles interacting with a medipix2 and a timepix devices. *Nuclear Instruments and Methods in Physics Research Section A: Accelerators, Spectrometers, Detectors and Associated Equipment*, 633, 10 2008.
- [11] J. Bouchami, A. Gutiérrez, T. Holy, A. Houdayer, J. Jakubek, C. Lebel, C. Leroy, J. Macana, J.-P. Martin, S. Pospíšil, S. Prak, P. Sabella, and C. Teyssier. Measurement of pattern recognition efficiency of tracks generated by ionizing radiation in a medipix2 device. *Nuclear Instruments and Methods in Physics Research Section A: Accelerators, Spectrometers, Detectors and Associated Equipment*, 633:S187–S189, 2011. 11th International Workshop on Radiation Imaging Detectors (IWORID).
- [12] W. L. Bragg. The Specular Reflection of X-rays. *Nature*, 90(2250):410, December 1912.
- [13] L.R.P. Butler and K. Laqua. Nomenclature, symbols, units and their usage in spectrochemical analysis—ix. instrumentation for the spectral dispersion and isolation of optical radiation. *Spectrochimica Acta Part B: Atomic Spectroscopy*, 51(7):645–664, 1996.

- [14] Robert Chatelain. *Radio-frequency pulse compression for high-brightness ultrafast electron diffraction: design, characterization and application*. PhD thesis, Department of Physics, 2014.
- [15] Yu Chen, Qingyun Shi, Guorui Huang, Liang Feng, Shuang Wang, Yonghong Cheng, and Shulin Liu. Measurement of true secondary electron emission yields of kapton. In *2021 International Conference on Sensing, Measurement & Data Analytics in the era of Artificial Intelligence (ICSMD)*, pages 1–4, 2021.
- [16] T.S. Curry, J.E. Dowdey, and R.C. Murry. *Christensen's Physics of Diagnostic Radiology*. Lippincott Williams & Wilkins, 1990.
- [17] D. A. G. Deacon, L. R. Elias, J. M. J. Madey, G. J. Ramian, H. A. Schwettman, and T. I. Smith. First operation of a free-electron laser. *Phys. Rev. Lett.*, 38:892–894, Apr 1977.
- [18] Y. Ding, A. Brachmann, F.-J. Decker, D. Dowell, P. Emma, J. Frisch, S. Gilevich, G. Hays, Ph. Hering, Z. Huang, R. Iverson, H. Loos, A. Miahnahri, H.-D. Nuhn, D. Ratner, J. Turner, J. Welch, W. White, and J. Wu. Measurements and simulations of ultralow emittance and ultrashort electron beams in the linac coherent light source. *Phys. Rev. Lett.*, 102:254801, Jun 2009.
- [19] Raymond C Elton. *X-ray Lasers*. Elsevier, 2012.
- [20] Paul Emma, R Akre, J Arthur, R Bionta, C Bostedt, J Bozek, A Brachmann, P Bucksbaum, Ryan Coffee, F-J Decker, et al. First lasing and operation of an ångstrom-wavelength free-electron laser. *nature photonics*, 4(9):641–647, 2010.
- [21] P. P. Ewald, editor. *Fifty Years of X-Ray Diffraction*. Springer New York, NY, 1962.
- [22] Romain Ganter. Swissfel-conceptual design report. 2010.

- [23] M. Hagelstein, C. Ferrero, M. Sanchez del Rio, U. Hatje, T. Ressler, and W. Metz. Xafs with an energy-dispersive laue monochromator. *Physica B: Condensed Matter*, 208-209:223–224, 1995. Proceedings of the 8th International Conference on X-ray Absorption Fine Structure.
- [24] B.L. Henke, E.M. Gullikson, and J.C. Davis. X-ray interactions: Photoabsorption, scattering, transmission, and reflection at $e = 50\text{--}30,000$ eV, $z = 1\text{--}92$. *Atomic Data and Nuclear Data Tables*, 54(2):181–342, 1993.
- [25] Juanjuan Huang, Benedikt Günther, Klaus Achterhold, Yi-tao Cui, Bernhard Gleich, Martin Dierolf, and Franz Pfeiffer. Energy-dispersive x-ray absorption spectroscopy with an inverse Compton source. *Scientific Reports*, 10(1):8772, 2020.
- [26] S. Huang, Y. Ding, Y. Feng, E. Hemsing, Z. Huang, J. Krzywinski, A. A. Lutman, A. Marinelli, T. J. Maxwell, and D. Zhu. Generating single-spike hard x-ray pulses with nonlinear bunch compression in free-electron lasers. *Phys. Rev. Lett.*, 119:154801, Oct 2017.
- [27] Tetsuya Ishikawa, Hideki Aoyagi, Takao Asaka, Yoshihiro Asano, Noriyoshi Azumi, Teruhiko Bizen, Hiroyasu Ego, Kenji Fukami, Toru Fukui, Yukito Furukawa, et al. A compact x-ray free-electron laser emitting in the sub-ångström region. *Nature Photonics*, 6(8):540–544, 2012.
- [28] Jan Jakubek. Precise energy calibration of pixel detector working in time-over-threshold mode. *Nuclear Instruments and Methods in Physics Research Section A: Accelerators, Spectrometers, Detectors and Associated Equipment*, 633:S262–S266, 2011. 11th International Workshop on Radiation Imaging Detectors (IWORID).
- [29] Jan Jakubek, Andrea Cejnarova, Tomas Holy, Stanislav Pospisil, Josef Uher, and Zdenek Vykydal. Pixel detectors for imaging with heavy charged particles. *Nuclear Instruments*

- and Methods in Physics Research Section A: Accelerators, Spectrometers, Detectors and Associated Equipment*, 591(1):155–158, Mar 2008.
- [30] In Soo Ko, Heung-Sik Kang, Hoon Heo, Changbum Kim, Gyu-jin Kim, Chang-Ki Min, Haeryong Yang, Soung Youl Baek, Hyo-Jin Choi, Geonyeong Mun, et al. Construction and commissioning of pal-xfel facility. *Applied Sciences*, 7(5):479, 2017.
- [31] J. A. Koch, J. J. Lee, and M. J. Haugh. High miller-index germanium crystals for high-energy x-ray imaging applications. *Appl. Opt.*, 54(34):10227–10231, Dec 2015.
- [32] AM Kondratenko and EL Saldin. Generating of coherent radiation by a relativistic electron beam in an undulator. *Part. Accel.*, 10:207–216, 1980.
- [33] X. F. Li, A. L’Huillier, M. Ferray, L. A. Lompré, and G. Mainfray. Multiple-harmonic generation in rare gases at high laser intensity. *Phys. Rev. A*, 39:5751–5761, Jun 1989.
- [34] M. Loyd, V. Sedov, J. Beal, T. Visscher, C. Donahue, A. Khaplanov, and Y. Diawara. Optimizing the spatial resolution and gamma discrimination of sipm-based anger cameras. *Nuclear Instruments and Methods in Physics Research Section A: Accelerators, Spectrometers, Detectors and Associated Equipment*, 1069:169830, 2024.
- [35] K. Mahata, H.T. Johansson, S. Paschalis, H. Simon, and T. Aumann. Position reconstruction in large-area scintillating fibre detectors. *Nuclear Instruments and Methods in Physics Research Section A: Accelerators, Spectrometers, Detectors and Associated Equipment*, 608(2):331–335, 2009.
- [36] K Mathieson, M.S Passmore, P Seller, M.L Prydderch, V O’Shea, R.L Bates, K.M Smith, and M Rahman. Charge sharing in silicon pixel detectors. *Nuclear Instruments and Methods in Physics Research Section A: Accelerators, Spectrometers, Detectors and Associated Equipment*, 487(1):113–122, 2002. 3rd International Workshop on Radiation Imaging Detectors.

- [37] N. Michel-Hart and W.T. Elam. Low-energy shelf response in thin energy-dispersive x-ray detectors from compton scattering of hard x-rays. *Nuclear Instruments and Methods in Physics Research Section A: Accelerators, Spectrometers, Detectors and Associated Equipment*, 863:1–6, 2017.
- [38] Margaret M. Murnane, Henry C. Kapteyn, Mordecai D. Rosen, and Roger W. Falcone. Ultrafast x-ray pulses from laser-produced plasmas. *Science*, 251(4993):531–536, 1991.
- [39] T. Nakamura, T. Kawasaki, T. Hosoya, K. Toh, K. Oikawa, K. Sakasai, M. Ebine, A. Birumachi, K. Soyama, and M. Katagiri. A large-area two-dimensional scintillator detector with a wavelength-shifting fibre readout for a time-of-flight single-crystal neutron diffractometer. *Nuclear Instruments and Methods in Physics Research Section A: Accelerators, Spectrometers, Detectors and Associated Equipment*, 686:64–70, 2012.
- [40] T. Oudheusden, van. *Electron source for sub-relativistic single-shot femtosecond diffraction*. PhD thesis, Applied Physics and Science Education, 2010.
- [41] T Poikela, J Plosila, T Westerlund, M Campbell, M De Gaspari, X Llopart, V Gromov, R Kluit, M van Beuzekom, F Zappone, V Zivkovic, C Brezina, K Desch, Y Fu, and A Kruth. Timepix3: a 65k channel hybrid pixel readout chip with simultaneous toa/tot and sparse readout. *Journal of Instrumentation*, 9(05):C05013, may 2014.
- [42] Gale Rhodes. *Crystallography Made Crystal Clear. A Guide for Users of Macromolecular Models*. Academic Press, 1999.
- [43] David Rich, Diling Zhu, James Turner, Dehong Zhang, Bruce Hill, and Yiping Feng. The lcls variable-energy hard x-ray single-shot spectrometer. *Journal of Synchrotron Radiation (Online)*, 23(1), 1 2016.
- [44] Leonardo Rossi, Peter Fischer, Tilman Rohe, and Norbert Wermes. *Pixel Detectors: From Fundamentals to Applications*. Springer, 2009.

- [45] Robert Schoenlein, Thomas Elsaesser, Karsten Holldack, Zhirong Huang, Henry Kapteyn, Margaret Murnane, and Michael Woerner. Recent advances in ultrafast x-ray sources. *Philosophical Transactions of the Royal Society A: Mathematical, Physical and Engineering Sciences*, 377(2145):20180384, 2019.
- [46] Helmuth Spieler. *Semiconductor detector systems*. Oxford University Press, 2005.
- [47] Aishwarya Srinath, Kristina von Fieandt, Stefan Fritze, Leif Nyholm, Erik Lewin, and Rebecka Lindblad. Near-surface analysis of magnetron sputtered alcrnbyzrn high entropy materials resolved by haxpes. *Applied Surface Science*, 666:160349, 2024.
- [48] J. Paul van Schayck, Eric van Genderen, Erik Maddox, Lucas Roussel, Hugo Boulanger, Erik Fröjdh, Jan-Pieter Abrahams, Peter J. Peters, and Raimond B.G. Ravelli. Sub-pixel electron detection using a convolutional neural network. *Ultramicroscopy*, 218:113091, 2020.
- [49] Raquel M A Vaz, Paul W. May, Neil A. Fox, C Harwood, Vijay Chatterjee, James A. Smith, Colin J. Horsfield, Jon S. Lapington, and Sophie Osbourne. Measurement of the secondary electron emission from cvd diamond films using phosphor screen detectors. *Journal of Instrumentation*, 10:P03004 – P03004, 2015.
- [50] Zhijie Wang, Susheng Tan, and M. Ravi Shankar. Mechanically induced interaction between diamond and transition metals, 2023.
- [51] Liang Jie Wong, Nicholas Rivera, Chitraang Murdia, Thomas Christensen, John D. Joannopoulos, Marin Soljačić, and Ido Kaminer. Control of quantum electrodynamical processes by shaping electron wavepackets. *Nature Communications*, 12(1), March 2021.
- [52] Doctor X Works. Dc photogun, 2020. <https://drx.works/parts/steering-coil/> [Accessed: 2024-08-24].

[53] Doctor X Works. Dc photogun, 2020. <https://drx.works/parts/photogun/> [Accessed: 2024-08-24].

[54] Doctor X Works. Focussing coil, 2020. <https://drx.works/parts/focussing-coil/> [Accessed: 2024-08-24].